

**Assessment of the Potential for Micro Energy Harvesting in
a Fixed-Wing MAV Configuration**

Darío Manzano Martos

Thesis to obtain the Master of Science Degree in

Aerospace Engineering

Supervisor: Prof. Doutor João Manuel Melo de Sousa

Examination Committee:

Chairperson: Prof. Doutor Filipe Szolnoky Ramos Pinto Cunha

Supervisor: Prof. Doutor João Manuel Melo de Sousa

Member of the Committee: Prof. Doutor André Calado Marta

October 2014

Acknowledgements

I would like to thank my family, especially my parents Pepi and Jordi and my grandparents Nati and Francisco; they have made possible what I have accomplished during all these years.

I would like to thank my supervisor too, Professor João Melo de Sousa for his help and advice during the development of the thesis.

Abstract

The weight limitations in Micro Aerial Vehicles (MAV) reduce their flight range and the operation time of on-board electronics. The use of electric batteries is essential in such vehicles, but their weight increases with increasing capacity, if the same type of battery is considered. The ability of charging the batteries in flight would, in principle, allow MAV to perform long endurance missions. A possible solution for the foregoing problem consists in the implementation of a technology known as “micro energy harvesting”. Although other transduction mechanisms may also be considered, this project focuses in the study of small piezoelectric elements/devices such as cantilever beams that would be installed on a fixed-wing MAV in order to convert aero-elastic vibrations into electric power. Such vibrations come from structural origin, due to boundary layer or large-scale turbulence, or simply from convection currents as a result of the presence of thermal gradients in the air. The simulation of these mechanisms is implemented using basic aerodynamic theories combined with an electromechanical model to achieve reliable data that may be used in a near future to perform a deeper investigation based on this topic.

Keywords: Micro Air Vehicle, Piezoelectricity, Micro Energy Harvesting, Cantilever Beam

Resumo

As limitações de peso em Micro Veículos Aéreos (MAV) reduzem a sua autonomia de voo e o tempo de operação dos dispositivos eletrônicos a bordo. O uso de pilhas elétricas é essencial em tais veículos, mas o seu peso aumenta com o aumento da respetiva capacidade, se o mesmo tipo de pilha for considerado. A capacidade de carregar as baterias em voo iria, em princípio, permitir aos MAV executar missões de longa duração. Uma possível solução para o problema anterior consiste na implementação de uma tecnologia conhecida como "micro-recolha de energia". Embora outros mecanismos de transdução possam também ser considerados, este projeto centra-se no estudo de pequenos elementos/dispositivos piezoelétricos do tipo "viga encastrada" que seriam instalados num MAV de asa fixa, a fim de converter as vibrações aero-elásticas em potência elétrica. Tais vibrações têm origem estrutural, devido à turbulência da camada limite ou das grandes escalas, ou simplesmente em correntes de convecção, como resultado da presença de gradientes de temperatura no ar. A simulação destes mecanismos foi implementada utilizando teorias fundamentais da aerodinâmica combinadas com um modelo electro-mecânico de modo a conseguir dados fiáveis que possam ser utilizados num futuro próximo em investigações mais profundas com base neste tema.

Palavras-chave: Micro-Veículo Aéreo, Piezoelectricidade, Micro-Recolha de Energia, Viga Encastrada

Contents

- 1 State of the art and objectives of the project 1**
 - 1.1 UAVs and MAVs..... 1
 - 1.2 Approaches for extended endurance..... 3
 - 1.2.1 Micro-engines..... 3
 - 1.2.2 Solar harvesters..... 5
 - 1.2.3 Piezoelectric harvesters 5
 - 1.3 Objectives of the project..... 9

- 2 Design requirements..... 10**
 - 2.1 MAV design conditions..... 10
 - 2.2 Materials..... 11
 - 2.3 Piezoelectric modes..... 12
 - 2.3.1 {3-1} Mode layout..... 13
 - 2.3.2 {3-3} Mode layout..... 13
 - 2.3.3 Comparison between modes 15

- 3 MAVs endurance 16**
 - 3.1 Endurance formulation 16
 - 3.2 Normalized endurance 18

- 4 Embedded piezoelectric device approach 20**
 - 4.1 Piezoelectric constitutive equations 20
 - 4.2 Electromechanical model..... 22
 - 4.2.1 Governing equations 22
 - 4.2.2 Modal analysis: Simple bending beam..... 27
 - 4.2.3 Modal analysis: Bending beam adding a tip mass..... 30

- 5 Results..... 33**
 - 5.1 Accelerations on the MAV..... 33
 - 5.2 Material selection..... 35
 - 5.3 Geometry adjustment 41
 - 5.4 Performance results 47

5.5	Evaluation of the solution	49
5.6	Validation	50
6	Theoretical approach on an external device configuration.	54
6.1	Initial planned solution.....	54
6.2	Other studies.....	55
6.2.1	Double-Lattice method for aero-elastic vibrations modeling.....	55
6.2.2	T-shaped cantilevers subjected to an air stream	56
6.3	Feasibility of the configuration.....	56
7	Conclusions and future work	59
	Bibliography.....	61
A.	ANNEX : Electrical connection for cantilevered harvester	63
A.1.	Series connection	66
A.2.	Parallel connection.....	67
B.	ANNEX : Validation of the code	69

List of Figures

Figure 1.1 Current MAV performance and desired target, courtesy of <i>Pines et al</i> [1]	2
Figure 1.2 Mass fractions for different air vehicles, Courtesy of <i>Pines et al</i> [1].....	2
Figure 1.3 Micro gas turbine generator cross-section, extracted from [2]	4
Figure 1.4 Micro -bipropellant rocket engine layout, extracted from [2]	4
Figure 1.5 Piezoelectric device used to harvest energy from walking, courtesy of [3].....	6
Figure 1.6 Location of the piezoelectric device behind the shoe, courtesy of [3]	6
Figure 1.7 Standard interface circuit	7
Figure 1.8 Switch Synchronized charge extraction.....	7
Figure 1.9 SSHI interface in parallel (left) and series (right) connection.....	8
Figure 2.1 {3-1} mode configuration (uni-morph case).....	13
Figure 2.2. Interdigitated electrodes in a piezoelectric harvester (yellow components)	14
Figure 2.3 Transversal view of a harvester in {3-3} configuration.....	14
Figure 2.4 {3-3} mode layout assuming simplifications.....	14
Figure 4.1 Layout of the internal harvester. Black layers represent electrodes, white structural material and grey piezoelectric material	20
Figure 4.2 Positive poling (left) and negative poling direction (right). Black layers represent piezoelectric material being used as electrodes	22
Figure 4.3 Layout of the bending beam with added tip mass. Image extracted from [12]	30
Figure 5.1 Layout of the wing surface used to extract fluctuations of C_L and C_D	33
Figure 5.2 Simulation, C_L and C_D with respect to time	34
Figure 5.3 Simulation frequency spectrum	34
Figure 5.4 Simulation outputs, lift, drag and total force	35
Figure 5.5 Layout of the harvester for material testing. White layer represent structural material and green represents piezoelectric material	37
Figure 5.6 Power vs. frequency at RI_{sc} for each material, short circuit case.	38
Figure 5.7 Power vs. frequency at RI_{oc} for each material, open circuit case.	38
Figure 5.8 Comparison of natural frequencies for PZT 5J (left) and PZT 4D (right)	39
Figure 5.9 Power vs. resistive load varying the frequency of excitation.....	39
Figure 5.10 Accurate swept of frequencies vs. resistive loads.....	40
Figure 5.11 Power vs. frequency for nine different devices	42
Figure 5.12 Frequency vs. tip length	44
Figure 5.13 Power vs. tip length	44
Figure 5.14 Resistive load vs. tip length	44
Figure 5.15 Frequency vs. tip mass for a non-fixed total length	45
Figure 5.16 Endurance improvement vs. mass of the MAV, using normalized endurance expression	47
Figure 5.17 Increment of the endurance vs. the total mass of the MAV	49
Figure 5.19 Power vs. Frequency from <i>Wang et al</i> [16] study of a cantilever harvester.....	52
Figure 5.22 Normalized endurance vs. added mass by the harvester	53

Figure 6.1 Layout of the T-shaped cantilever beam from <i>Kwon</i> [19].....	56
Figure 6.2 Output performance for a T-shape device with 6Hz vibrations from <i>Kwon</i> [19].....	57
Figure 6.3 Power vs. wind speed comparison from <i>Kwong</i> [19].....	57
Figure A.1 Layer disposition of uni-morph cantilevered harvester.....	64
Figure A.2 Layer disposition of the bi-morph cantilevered harvester	64
Figure A.3 Series connection for a bi-morph harvester	66
Figure A.4 Parallel connection of a bi-morph harvester	67
Figure B.1 Table showing the parameters for the device simulation, courtesy of <i>du Toit</i>	69
Figure B.2 Comparison of the power output vs. resistive load for different frequencies. Thesis results on the left and original simulation on the right.....	71
Figure B.3 Comparison of the voltage output vs. resistive load for different frequencies. Thesis results on the left and original simulation on the right.....	73
Figure B.4 Comparison of the tip displacement output vs. resistive load. Thesis results on the left and original simulation on the right	75

List of Tables

Table 1.1 MAV ideal design requirements 1

Table 2.1 MAV performance properties [1] 10

Table 2.2 Starting parameters for early designs 11

Table 2.3 Charge coefficient of synthetic ceramics..... 11

Table 2.4 Results comparing the performance between piezoelectric modes {3-1} and {3-3} 15

Table 5.1 Parameters of the lifting surface 33

Table 5.2 Parameters of the piezoelectric material test. Last three parameters vary with the chosen material 36

Table 5.3 Geometric dimensions for different harvesters 41

Table 5.4 Output results for the different harvesters..... 42

Table 5.5 Parameters set for harvester G1 tests..... 43

Table 5.6 Geometry and output results with tip mass..... 43

Table 5.7 Geometrical parameters of the proposed harvester 46

Table 5.8 Output values of the proposed harvester 46

Table 5.9 Vehicle mass fractions for three MAV and the fractions adjusted for the study 47

Table 5.10 Parameters for a cantilever harvester simulation in *Wang et al* [16]..... 51

Table 5.11 Physical properties of the piezoelectric devices considered in *Anton et al* [13]..... 52

Table 5.12 Physical properties of the piezoelectric devices designed in this project 52

List of Symbols

Symbol	Description	Units
A	area	[mm ²]
a_{base}	base acceleration range for harvester design	[m/s ²]
B_f	modal forcing matrix with elements i, j	[kg]
b	scalar modal forcing coefficient	[kg]
b	width of the structure	[m]
C	damping coefficient	[N·s/m]
c	chord	[m]
C_L	lift coefficient	-
C_D	drag coefficient	-
C_P	capacitive coefficient	[F]
D	electric displacement	[C/m ²]
d	piezoelectric constant	[m/V]
E	electric field	[V/m]
E_B	energy provided by batteries	
e	piezoelectric constant matrix	[C/m ²]
e_b	specific energy from MAV batteries	[J/kg]
f	frequency	[Hz]
i	intensity	[μA]
I	second moment of area of structure	[m ⁴]
J_{yy}	proof mass moment of inertia about the center of gravity	[kg/m ²]
J_0	proof mass moment of inertia about the lading point	[kg/m ²]
K	stiffness of the structure	[N/m]
k_{ij}	electromechanical material coupling	-
L	length	[mm]
L	lift	[N]
M	mass of structure	[kg]
m	mass per length	[kg/m]
m_b	mass of the batteries	[kg]
nf	number of discrete external forces applied	-
nq	number of electrode pairs	-
nr	number of bending modes	-
O	location proof mass loading on cantilevered structure	-
o_x	horizontal distance from O to proof mass center of gravity	[m]
o_z	vertical distance from O to proof mass center of gravity	[m]
P	poling direction	[C/m ²]
P_{out}	electrical power generated	[μW]
P_{dens}	specific power density	[μW/m ³]
q	charge	[C]
R	resistance	[Ω]
r	generalized mechanical coordinate	[m]
S	strain vector	[m/m]
S	wet surface area	[m ²]
T	stress vector	[N/m ²]
T_k	kinetic energy	[J]
T_R	thrust required for a level flight	[N]
t	thickness	[mm]
t	time	[s]
t_E	endurance	[min]

U	potential energy	[J]
u	mechanical relative displacement	[m]
v	voltage across element pair	[V]
V	volume	[m ³]
V_{out}	voltage generated or extracted	[V]
V_{∞}	free stream velocity	[m/s]
W	external work	[J]
	weight of the MAV	[N]
W_{harv}	weight of the harvester	[N]
W_e	electrical energy	[J]
W_{ST}	MAV structure weight	[N]
W_T	total weight of the MAV without harvester	[N]
w	absolute displacement	[m]
x_i	cartesian coordinate directions with $i=1,2$ or 3	-
x_a	general beam structure axial coordinate	-
x_t	general beam structure thickness coordinate	-
z	relative displacement	[m]
α	dimensionless time constant	-
Δ	aspect ratio	-
η_P	efficiency of the propulsion system of the MAV	-
ε	permittivity	[F/m]
κ	electromechanical structure/system coupling	-
λ_N	modal analysis constant	-
∇	gradient of variable	[m ⁻¹]
Ω	frequency normalized to resonance(short -circuit) frequency	-
ω	operating frequency	[Hz]
ω_N	natural frequency	[Hz]
φ	scalar electrical potential	-
ψ_r	mechanical mode shape vector of elements $\psi_{r,t}$	-
ψ_v	electrical mode shape vector of elements $\psi_{v,j}$	-
ρ	density	[kg/m ³]
Θ	coupling coefficient matrix with elements θ_{ij}	-
θ	scalar coupling coefficient	-
ξ	mechanical damping ratio	-
Subscripts		
0	proof mass property or variable	-
1,2	piezoelectric element numbers	-
ar	variable evaluated at anti-resonance frequency	-
e	electrical domain parameter	-
eff	effective parameter	-
l	electrical load	-
N	mode number during analysis	-
opt	power-optimized parameter	-
p	piezoelectric material or element property	-
r	variable evaluated at resonant frequency	-
s	structural layer or section property	-
t	variable at the tip of the structure/beam	-
$T/total$	total	-
sc/oc	short/open circuit	-

Superscripts

<i>t</i>	transpose matrix or vector	-
<i>E</i>	variable at constant electric field	-
<i>D</i>	variable at constant electric displacements	-
<i>T</i>	variable at constant stress	-
<i>S</i>	variable at constant strain	-

1 State of the art and objectives of the project

This chapter is an introduction about the ongoing advances in unmanned vehicles design which includes the status of the UAVs (Unmanned air vehicles) and MAVs (Micro air vehicles) performance, future goals and current alternative ways to increase the endurance such as micro fuel powered engines and electric harvesters. Because of the aim of this project, there is a deeper explanation on piezoelectric harvesters. The knowledge about the current uses and studies of piezoelectric devices is extremely useful since it gives the notions about the output power quantities, difficulties on building devices and discard some approaches that in principle may be a plausible option to implement on MAVs. At the end, the reader will find also a section containing the steps followed for the development of the thesis detailing the objectives and aim of each one of them.

1.1 UAVs and MAVs

UAVs are certainly a kind of air vehicle that has captured the attention of a significant amount of aeronautic researchers. The reason of their success is the capability of these vehicles to gather data, provide surveillance and explore in hostile, unknown or unreachable terrains. That combined with their relatively low manufacturing cost has encouraged the creation of UAV programs worldwide. However a new class of UAV has emerged which is an order of magnitude smaller in length and two order of magnitude lighter in weight. This new class is called micro air vehicle (MAV). These vehicles have been defined to have no length dimensions greater than 15 cm with a gross take-off weight of approximately 200g or less. A summary of an MAV ideal design requirements is presented in Table 1.1

Specification	Requirements	Details
Size	<15 cm	Maximum dimension
Weight	100g (aprox.)	Objective GTOW
Range	1 to 10 km	Operational range
Endurance	60 min	Loiter time on station
Altitude	<150 m	Operational ceiling
Speed	15 m/s	Maximum flight speed
Payload	20g	Mission dependent
Cost	1500 USD	Maximum cost

Table 1.1 MAV ideal design requirements

As a new class of air vehicle, these systems face many unique challenges that make their design and development difficult, like the aerodynamic behavior of the lifting surfaces over a low Reynolds flow. This condition produces complex phenomena difficult to describe with analytic methods. Improving

the endurance is another major issue concerning the MAV design due to the necessity of improving the performance for longer missions without penalize on the dimension requirements.

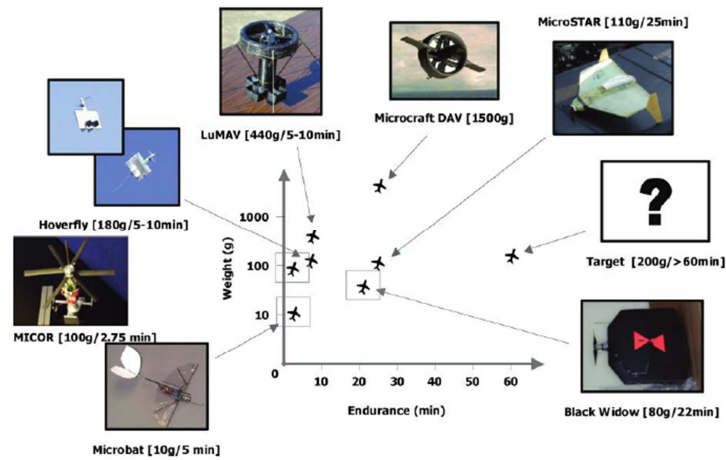


Figure 1.1 Current MAV performance and desired target, courtesy of Pines et al [1]

Specifically focusing on the endurance issue, ongoing projects are trying to build MAVs capable to flight for more than an hour, which is more than twice the endurance of the current designs performance. Figure 1.1 shows current projects and the point of ideal requirements, which is also the ideal target used to achieve the goal of this thesis. Endurance of a vehicle is inversely proportional to the power required to maintain steady state level which implies the necessity to minimize the power required to increase the endurance. Compared to full-scaled aircrafts, MAVs use a higher percentage of propulsion mass. See Figure 1.2 comparing the mass fraction of three different MAVs compared to a Boeing 767.

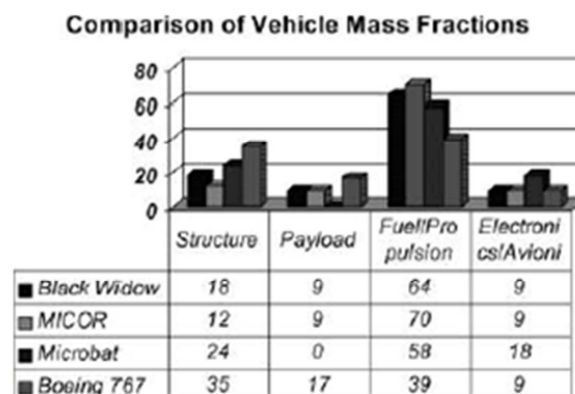


Figure 1.2 Mass fractions for different air vehicles, Courtesy of Pines et al [1]

Note how the three micro vehicles use an extra 20% on propulsion mass fraction than the full scale aircraft while the structure fraction shows the inverse situation, large aircrafts use between 10% and

15% more structural mass than the MAVs. This fact leads to think about the use of power sources able to provide higher energy density $\left(\frac{\text{Energy}}{\text{prop.mass fract}}\right)$ or even better, a double function: a structure able to provide power as well.

1.2 Approaches for extended endurance

There are different approaches to improve the endurance problem; this chapter presents different options taking a deeper look into electric harvesters. The reader shall take a look at the current trends to be aware of the effort put in reach better results and to point the variety of alternatives that are being explored. This may help as well to clarify the aim of the current project and the motivation on keeping developing solutions for future projects.

1.2.1 Micro-engines

There is a solid base on developing air vehicles based on fossil fuel propulsion. For UAVs, air-breathing engines are still an option because there are no dimension limitations. Instead, for MAVs using the same technology become a hard work. Nevertheless, there are current projects working on the development of micro-scaled¹ fuel engines. MIT is currently developing micro-gas turbines of 1cm diameter by 3mm thick using semiconductor materials and using the MEMS (Microelectromechanical systems) technology. These engines are designed to produce 10-20W of electric power or 0,05-0,1 N of thrust while consuming under 10 g/h of H₂.

The primary application for these systems is to be able of recharging batteries. In general, tens of watts of electric power are enough to charge many portable devices. Besides, the energy density of a liquid hydrocarbon fuel is 20-30 times that of the best battery technology so the size of the power source can shrink simultaneously. If there are other systems that need more power than one single engine can provide, then several can be used in parallel. One convenient way of implementing this parallelism would be connect them using a wafer plate as the substrate to integrate the whole system, e.g. including the interconnecting fuel and control lines on the fabrication wafer. Such a wafer, 200 mm diameter by 3 mm thick, could produce as much as 10 kW of power. Since its power-to-weight ratio is so high, one attractive use of such an array would be for distributed, compact, highly redundant auxiliary power units in air and land vehicles.

Another use for micro-gas turbine engines is vehicle propulsion. The output of a single engine is sufficient for the micro-aircraft of current interest, with gross takeoff weights of 50-100 g. When

¹ The term micro-scale may not be really accurate since the dimensions of the engine are noticeable with the human eye, however the MEMS technology is used to produce the different elements of the engine, and this is why prefix *micro-* is used.

more thrust is needed, multiple engines or wafers can be used. A 200 mm diameter wafer may produce 95 N of thrust. Another advantage of a micro-engine approach to propulsion is that thrust is truly modular, so one engine design can be used over a wide range of vehicles and thus be produced in large quantity. Also, an increase in vehicular thrust requirements would be met simply by adding more engines, rather than the current practice of modifying or redesigning the engine. Figure 1.3 shows the layout of a micro-engine:

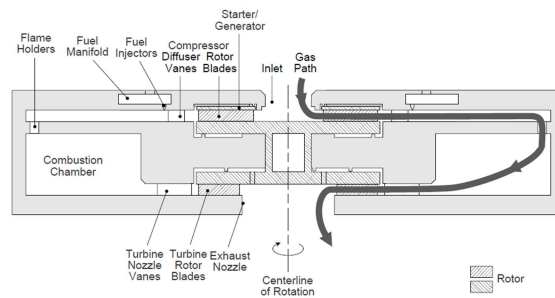


Figure 1.3 Micro gas turbine generator cross-section, extracted from [2]

Similarly to the micro gas turbine, there is another device under development: The micro-bipropellant rocket engine. The engine consists of a regenerative cooled chamber and nozzle, pumps, controls, and plumbing. The engine configuration is prismatic 2-D structure to be compatible with current fabrication technology (see Figure 1.4). This requires all of the nozzle expansion to be in-plane so it is the nozzle exhaust area which limits the engine power that can be fit onto a chip rather than propellant pumping capability. There are several options for producing much larger thrusts if needed, including: stacking motors together; placing only the pumps, controls and chamber on a chip and mating one or more such chips to a conventionally fabricated large exhaust nozzle; or placing only the pumps and controls on a chip and feeding a conventional chamber and nozzle.

Single engine applications might include spacecraft attitude control and station keeping. Arrays of 20-50 engines could be used for apogee kick. Larger arrays might be used for main propulsion for very small launch vehicles. In this application, differential throttling across the array could provide thrust vector control.

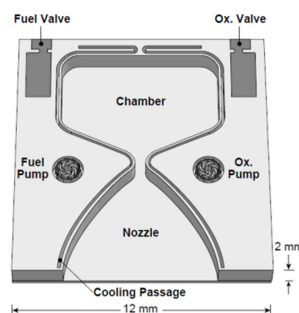


Figure 1.4 Micro-bipropellant rocket engine layout, extracted from [2]

1.2.2 Solar harvesters

Probably the most used harvesters intended to cover vehicle applications (among other rather more conventional applications) are the solar harvesters. Its notorious advantages in large scale aerial vehicles have granted them deeper investigations to achieve better results in new MAV projects until limits such as create UAVs capable of flying continuously without any other source of energy. The photoelectric effect is well studied and hence difficult to find quick and reduced cost improvements to apply on MAVs. However, for aviation projects like MAV or UAV the goal is to design aircrafts that complement the use of the solar harvesters in order to preserve the gathered energy for situations where is not possible to use solar arrays. Those situations would be the night time or environment difficulties such as dense clouds. That is why the majority of the ongoing projects of solar MAVs are focused in high altitude flights, where the resistance is lower; the atmospheric events such as winds, clouds and storms are unlikely to happen and the endurance can be increased in great amount if the aircraft counts on a well planned design. High aspect ratio is then, the common choice when designing solar powered aircrafts.

The technology is suitable for MAVs too but there are some restrictions that make difficult to use it in the same ways as UAVs do. The size reduction is one of them; the batteries are small and cannot store as much energy as larger aircrafts but in daylight operation is a helpful solution for the endurance issues. The propulsion power makes difficult for these vehicles to fly at high altitudes and electronic devices like cameras do not have enough capacities to perceive the terrain at long distances, hence MAVs are forced to flight at low altitudes and are exposed to adverse atmospheric events which reduce considerably the flight time. Larger panels are needed to achieve the desired 60 min flight time but then more surface is needed which translates into bigger airplanes leaving consequently the scale of MAV sized vehicles. MAV projects like the HORNET and WASP from DARPA agency use solar cells on top of the wing but neither of them have report significant results compared with the rest of MAV models without harvesting systems.

1.2.3 Piezoelectric harvesters

Nowadays, solar/wind harvesters and electric energy seems to be the most common way to collect energy because of the uses in macroscopic scale. However, the piezoelectricity is becoming a trend due the multiple uses for the new technologies. That is the case of sensors, the great part of tools for measuring physical variables such as pressure, speed, temperature, accelerations and other quantities are based on piezoelectric devices. And more important than the implementation of this effect is the fact that these harvesters can be “easily” designed with small dimensions thanks to the MEMS technology.

Indeed, to improve the efficiency of devices (not only MAVs) that require small power sources, it is vital to reduce the mass of the harvesters as well as to provide the highest possible power density. Piezoelectric materials seem to have enough specific power $\frac{W}{kg}$ to capture small movements, since currently their main application is to amplify signals of transducers, and produce a voltage that can be measured but it is not so clear that this energy could be stored with profitable benefits. A lot of effort and creativity has been put together to find out whether it is a sensible solution or these applications suit better for other materials rather than piezoelectric.

A first example of piezoelectric harvester is a shoe-mounted device to scavenge electricity from the forces exerted on the shoe during walking. Studies made by T.Staner [3] have concluded that power generation through walking can easily generate power when needed, and 5-8W of power may be recovered while walking at a brisk pace. Afterwards, further researches on improvement in the structures and circuits for shoe-mounted devices have been published. Figures 1.5 and 1.6 show the device and the location on the shoe:

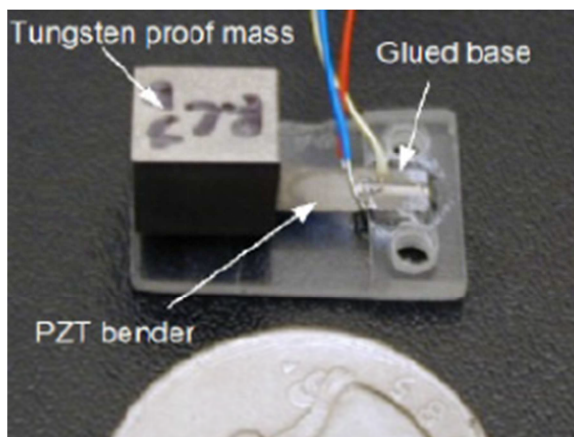


Figure 1.5 Piezoelectric device used to harvest energy from walking, courtesy of [3]



Figure 1.6 Location of the piezoelectric device behind the shoe, courtesy of [3]

Another example is the device proposed by S.Roundy and P.K. Wright [3] who demonstrated a vibration based piezoelectric generator. The device is a cantilever beam type with proof mass to adjust the resonance frequency. An optimized design demonstrated that the device was able to produce enough power to run a custom designed 1.9 GHz radio transmitter from a vibration induced by a base acceleration of 2.5 m/s^2

Not only the device design is important to study the viability of the piezoelectric harvesters, but the electric circuit is also a topic well studied because is the responsible for collecting the energy and transport it to the batteries. Another remarkable fact about harvesting the energy via vibrations is that since the mechanical vibration of the piezoelectric element generates an alternating voltage

across its electrodes, most of the proposed electrical circuits include an AC-DC converter to provide the electrical energy to its storage device, as illustrated in Figure 1.7.

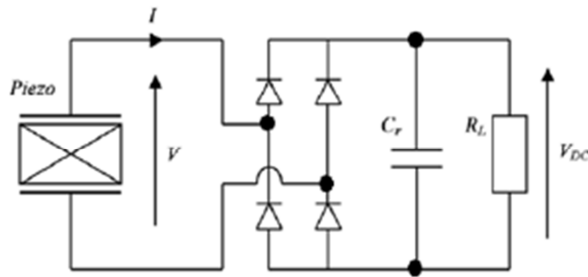


Figure 1.7 Standard interface circuit

Researches such as the proposed by Guyomar *et al* [4], Lefeuvre *et al* [5] and Badel *et al* [6] have developed a new flow optimization principle based on the extraction of the electric charge produced by a piezoelectric element, synchronized with the mechanical vibration operated at the steady state, as shown in Figure 1.8. They have claimed that the harvested electrical power may be increased by as much as 900% over the standard technique.

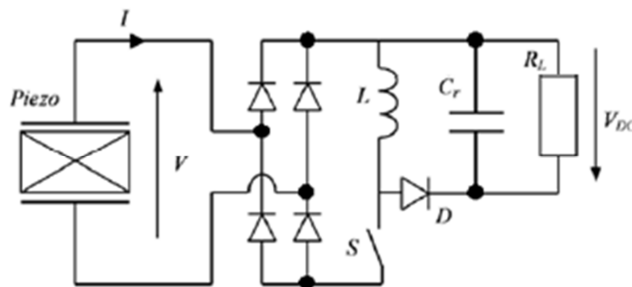


Figure 1.8 Switch Synchronized charge extraction

A similar model that has also been studied and its performance analyzed, is known as synchronized switch harvesting on inductor (SSHI) (see Figure 1.9) and seems to present a similar behavior to that of the electrical response produced by the standard interface model in a strongly coupled electromechanical system operated at short circuit resonance.

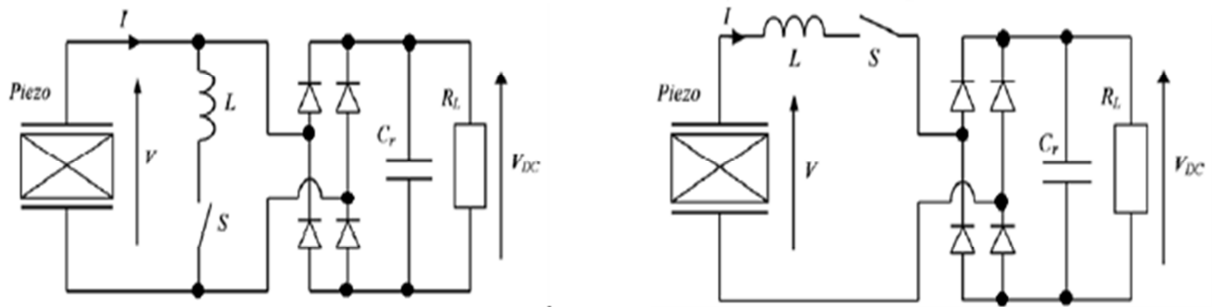


Figure 1.9 SSHI interface in parallel (left) and series (right) connection

Because of the concern about the dimensions of the harvesters, it is fair to end this section with a last harvester developed by *Jeon et al* [7] who successfully created the first MEMS based micro-scale power generator using mode {3-3}² of PZT material in 2005 . The device is a cantilevered beam of $2000 \mu\text{m} \times 500 \mu\text{m}$ and $12 \mu\text{m}$ thick silicon layer with a $500 \mu\text{m} \times 500 \mu\text{m}$ tip mass which generated $1.15 \mu\text{W}$ of effective power when connected to a $20,4\text{k}\Omega$ resistance load leading to a 432mV AC voltage. An improved device was announced later that under the 608Hz resonant frequency, the device generated about $0,89 \text{V}$ AC peak–peak voltage output to overcome germanium diode rectifier toward energy storage. The power output obtained was of $2.16 \mu\text{W}$.

As the reader can appreciate, the studies of piezoelectric harvesters are a relatively new trend but the power that can be extracted from them show great amount of possible applications even though in a larger scale may not be the first option.

Previous work done by the researchers provides initial useful information to build the guidelines of future projects, allow the evaluation in a first approximation of the problem and determine in which direction the new investigations (about the same or similar topics) could be started. That is the case of this project, and as far as it has been explained the application of this technology to small unmanned vehicles seems to be a powerful solution for the energy efficiency issues. It also may occur that the use of piezoelectric harvesters could be restricted to certain conditions making difficult the implementation of these devices on MAVs.

² Refer to section 3 to understand the meaning of mode {3-3} on a piezoelectric harvester

1.3 Objectives of the project

In view of the previous information, this report has been structured following a typical design scheme. That is, identifying the needs of the problem, bounding key parameters to create a basic layout of the solution and testing the proposed concept (looping if necessary) until it is adjusted for an optimal performance. Each chapter has particular objectives; the achievement of these objectives provides advances in the study. In the end, every partial result and study will lead to the final solution and conclusions. The approach described above will be developed in the next chapters.

The following chapter to proceed with the identification of the problem requirements; the goal here is to bound the performance of the harvester in order to adapt it to the problem specifications. Subsequently, two chapters include the modeling of the MAVs endurance and the piezoelectric behavior of the harvester with a mathematical approach, giving the basis to carry out simulations on future harvester designs and connecting both the parameters aimed to be improved and the piezoelectric inputs. At last, a chapter to describe the results of the design process, showing how the tests were performed and how the final harvester evolved since the first concept until the last version.

An extra chapter is also dedicated to a theoretical approach on the design of an external harvester.

2 Design requirements

The design of piezoelectric harvesters is subjected to several restrictions because they depend on external factors to collect the energy. The current work aims to install them into MAVs to take advantage of the vibrations. Nevertheless, vibrations are not the only important aspect to achieve an optimal design, materials, layout and/or configuration of the device as well as the mission to be performed by the MAV could affect the performance of the harvester.

The next lines will show which are the key parameters needed to make the preliminary designs and check the viability of using piezoelectric harvesters to improve MAVs performance.

2.1 MAV design conditions

An important requirement of the project is fix the design conditions at cruise stage of the flight which is most of the mission time (since MAV are almost exclusively designed for reconnaissance missions). Their small size and limited weight cannot allow them to perform complex tasks but this limitation is actually an advantage because the harvester will be working during the majority of the mission at design conditions. Table 2.1 shows some MAV models and their respective performance parameters.

Properties	Black Widow	Hoverfly	LUMAV	MicroStar	Microbat	MICOR
Fixed wing	Yes	No	No	Yes	Yes	No
GTOW (g)	80	180	440	110	10.5	10.3
Cruise Speed (m/s)	13.4	15-20	5	13.4-15.6	5	2
Max L/D	6	N/A ³	N/A	6	N/A	5
Endurance (min)	30	13.2	20	25	2.25	3
Power Source	Li-ion Batteries	Li-ion Batteries	2-stroke IC engine	Li-ion Batteries	NiCad N-50 cells (Sanyo)	Li-ion Batteries
Energy density (W·h/kg)	140	140	5500 methanol	150	100	150

Table 2.1 MAV performance properties [1]

Fixed wing MAVs are the priority because this project is focused on this configuration. Notice the similarities between MicroStar and Black Widow; their parameters are the base to begin the design because they are able to actually perform a mission. Microbat has a remarkably reduced endurance and low weight that makes him stay out of the MAV requirements. Comparing performance with both fixed wing and hover MAVs two different group can be made, that is by comparing the flight time. In fact, endurance between 10 and 30 minutes are low but acceptable values to work with, while flight times between 2 and 5 minutes are not. This means that preliminary values for the rest of the performance parameters are chosen in accordance to endurance values around 20 minutes. Table 2.2 shows the values accepted for a starting point with some thresholds to adjust if it is necessary.

³ N/A: Not available

	Fix. Wing	GTOW (g)	Cruise Speed (m/s)	Max. L/D	Endurance (min)	Power source	E. Density (W·h/kg)
main	Yes	125	15	6	20	Battery + harvesters	140 +harv. Energy Density
Min.	-	100	14	5.5	15	-	-
Max.	-	180	20	7	25	-	-

Table 2.2 Starting parameters for early designs

2.2 Materials

There are several piezoelectric materials on the market but only a few of them are acceptable for the purpose of the project. Certain parameters of these materials are more valuable than others and the value of these particular properties depend on their physical and chemical constitution. There are natural and synthetic crystals and even though crystals like quartz show high output voltage, natural materials will not be a smart solution because they need to be subjected to high forces $\sim [kN]$ (and/or accelerations) plus it is needed a big amount of the material which translate into extra weight. These facts make impossible to apply these crystals to the current problem.

Then the best solution is to choose synthetic crystals, in particular ceramic materials. The properties that make them valuable are the piezoelectric coefficients⁴ δ_{ij} , g_{ij} , e_{ij} and h_{ij} . The first one (d_{ij}) is the most relevant because is related with the direct effect⁵ of the piezoelectricity: the higher the value of d_{ij} the higher voltage obtained and the higher the power that can be reached from the harvester.

Ceramic crystals are distributed in different sub-groups by chemical composition:

- **Barium-Titanate** ($BaTiO_3$): First piezoelectric ceramic discovered
- **Bismuth-Titanate** ($Bi_4Ti_3O_{12}$)
- **Lead Zirconite Titanate** ($Pb[Zr_xTi_{1-x}]O_3$): Known as PZT is the most common piezoelectric ceramic used today
- **Potassium niobate** ($KNbO_3$)
- **Lithium niobate** ($LiNbO_3$)
- **Lithium tantalate** ($LiTaO_3$)

Coefficient	PZT	Ba-Titanate	Bi-Titanate	Li-Niobate	Li-Tantalate
d_{31}	-250	-30	-2,5	-2	-0.85
d_{33}	700	145	140	8	16

Table 2.3 Charge coefficient of synthetic ceramics

From the previous list, Lead Zirconite Titanate (PZT) based devices are the best option to obtain positive results in terms of power output. See also Table 2.3 where the largest charge coefficients correspond to PZT ceramics. This compound is used in a large variety of sensors not only for its

⁴ See section 5.1 to have deeper understanding about the meaning of the coefficients

⁵ Direct piezoelectric effect is obtain an output voltage after apply a stress to the material

piezoelectric properties but for the pyro electric effect and its large dielectric constant. It is usually not used in its pure form, rather it is doped with either acceptor dopants, which create oxygen (anion) vacancies, or donor dopants, which create metal (cation) vacancies and facilitate domain wall motion in the material. In general, acceptor doping creates hard PZT while donor doping creates soft PZT. Hard and soft PZT's generally differ in their piezoelectric constants. Piezoelectric constants are proportional to the polarization or to the electrical field generated per unit of mechanical stress, or alternatively is the mechanical strain produced per unit of electric field applied. In general, soft PZT has higher piezoelectric constants, but larger losses in the material due to internal friction. In hard PZT, domain wall motion is pinned by the impurities thereby lowering the losses in the material, but at the expense of a reduced piezoelectric constant. The bibliography includes catalogs of PZT model materials that show their properties [8] [9] [10] [11].

The other materials listed before are also commonly used but each one for specific applications. That is one of the main differences with PZT, these materials cannot be as easily adapted to other applications. Barium titanate sometimes replace PZTs as a dielectric materials, bismuth titanate has its best performance in application at high temperatures where is able to reach similar charge coefficients to those of the PZTs. Lithium niobate is used extensively in the telecoms market and is the material of choice for the manufacture of surface acoustic wave devices, those surfaces are used to build filters or DC to DC converters. Sometimes lithium niobate can be replaced with lithium tantalate as well. Finally Potassium niobate has nonlinear optical coefficient properties, making it common in the manufacture of lasers. The cost of these materials is similar except for those with high technology applications like potassium niobate. In terms of availability and manufacturing spectrum again PZT is the most advantageous material counting on different doped versions, plate dimensions or particular use for MEMS applications

Designing a harvester choosing only one kind of ceramic material would be simplistic but try every ceramic crystal would take a lot of time and effort that might be unnecessary. That is why in this section PZT has been discussed to be the best option. In the results, the reader will find graphics where different PZTs are compared to find an optimal output response.

2.3 Piezoelectric modes

There are two configurations considered in this project to design piezoelectric harvesters, depending on the direction between the strain applied and the direction of the electric field. The first configuration is called {3-1} and indicates that strain and electric field vectors are perpendicular. The second configuration is {3-3}, which indicates that both electric and strain vectors are parallel.

There are differences when deciding between {3-1} and {3-3} configurations for a device design but in general the piezoelectric effect is larger for {3-3} mode, as for most piezoelectric devices the ratio $\frac{d_{33}}{d_{31}} \sim 2.4$. [12]

At first glance, {3-3} mode seems to be the best option but there are some features that would make {3-1} mode a more successful choice. The first feature is the complexity of the manufacturing process, if there is a chance to use mode {3-1} and obtain outputs that satisfy the power requirements then there is no need to increase the cost of the product. Another issue is the model used to simulate the behavior of mode {3-3}, some assumptions have been made to simplify the equations and therefore the results obtained may not be as accurate as desired but it provides the order of magnitude, which is vital to know if this technology can be applied on MAVs. The following lines explain the layouts of both modes.

2.3.1 {3-1} Mode layout

This mode is the simplest configuration to design a vibration harvester. It is composed by 4 layers (basic configuration of the device) stacked up as shown in figure 2.1.

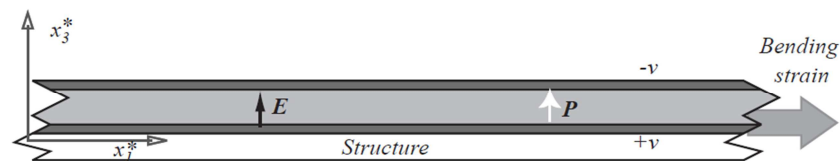


Figure 2.1 {3-1} mode configuration (uni-morph case)

The darker layers correspond to the electrodes, the grey layer represents the piezoelectric material and the white layer is the structural material. Although this configuration is used, there are other devices based on this configuration that include two piezoelectric layers, and therefore two more electrodes. This configuration is called bi-morph because of the symmetry with the x_1 axis. Note how the electric field vector is perpendicular to the bending strain allowing only the piezoelectric effect in 3-1 direction.

2.3.2 {3-3} Mode layout

This configuration is composed of interdigitated electrodes at the top of the piezoelectric layer so the total number of layers on the device is reduced to three. The alternative position between positive and negative electrodes (interdigitation) is achieved by superposing two main electrodes with segmented extensions oriented to the center of the beam. Figure 2.2 shows a general harvester using this configuration for a better understanding.



Figure 2.2. Interdigitated electrodes in a piezoelectric harvester (yellow components)

The green layer represents the piezoelectric material and the grey one is the structure layer. Now is easier to see that both electric field and strain act in the same direction, however the electric field does not act as a straight line because the disposition of the electrodes face the surface towards the piezoelectric layer instead of facing the complementary electrode. Looking at figure 2.3 it is clear that the electric field bends to in order to find the way to the other electrode. This fact makes the electromechanical modeling of this mode quite difficult.

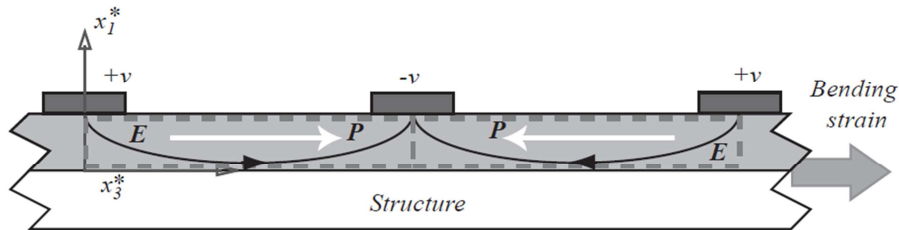


Figure 2.3 Transversal view of a harvester in {3-3} configuration

This is why certain assumptions are introduced as well as a variation of the electrode configuration to obviate theoretical problems. When working with this mode it will be assumed that the region of the piezoelectric element under the electrode is electrically inactive, whereas the section between the electrodes utilizes the full d_{33} effect. Physically, these considerations translate to figure 2.4.

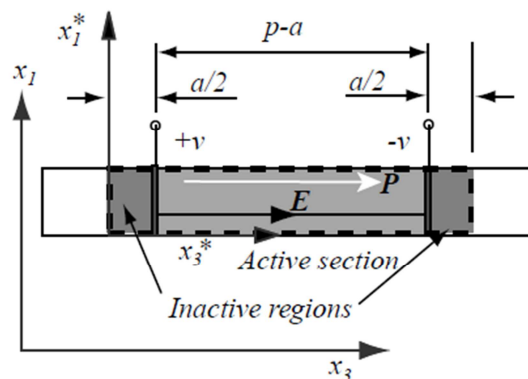


Figure 2.4 {3-3} mode layout assuming simplifications

2.3.3 Comparison between modes

Some bibliographical research [3] [12] has shown that even though mode 3-3 seem to enlarge the output of the harvester, the experimental performance results show a different behavior for some variables. In an experiment described by Wu *et al* [3], two MEMS generators, each one with a different configuration, were excited at 2g acceleration level. The measurements are summarized in table 2.3:

Mode	f_{res}	$R_{l_{opt}}$	P_{out}	$V_{out_{oc}}$	$V_{out_{wl}}$
3-1	255.9 Hz	150 k Ω	2.099 μW	2.415 V_{p-p}	1.587 V_{p-p}
3-3	214.0 Hz	510 k Ω	1.288 μW	4.127 V_{p-p}	2.292 V_{p-p}

Table 2.4 Results comparing the performance between piezoelectric modes {3-1} and {3-3}

For the same dimensions of the beam the output power for the {3-3} mode piezoelectric MEMS generator was smaller than that for the {3-1} mode piezoelectric MEMS generator. This was due to the PZT material of the {3-3} mode device which was poled using the interdigitated electrodes and which results in a non-uniform poling direction because the piezoelectric under the electrode is a region affected by the electric field. The material under the electrodes was not used because it was not poled correctly. Furthermore, the further the distance from the surface of the PZT material, the less effective the poling electric field strength will be. This causes an efficiency drop for the {3-3} mode piezoelectric MEMS generator when compared to the {3-1} mode piezoelectric MEMS generator. Nevertheless, the output voltage of the {3-3} mode piezoelectric MEMS generator was higher than that of the {3-1} mode piezoelectric MEMS generator and easily adjusted by the gap of the interdigitated electrodes under the same dimensions of the beam shape.

Talking about generators at a higher scale means that mode {3-3} efficiency would be even lower than that for the MEMS generator described in the previous lines. Then, designing a harvester to suit an MAV with this mode does not have a clear benefit over mode {3-1}. For this reason, in the development of this thesis only mode {3-1} is considered in the design of the harvester. Besides, the fabrication process cost of {3-3} configuration is higher than the {3-1} mode which means an extra expense with the only benefit of being able to adjust the output voltage in a more controlled way. But controlling the voltage will not be an important feature if the necessary power cannot be assessed to improve the MAV endurance. Mode {3-3} would be a good improvement in advanced stages of a possible harvester design where more accurate conditions are needed to perform an optimal output.

3 MAVs endurance

In order to design a device to improve MAV's endurance, there must be a criterion to evaluate how adding new components to a vehicle affects its maximum flight time. In fact, there are certainly known expressions to estimate the endurance of an aircraft such as the Breguet equation. This chapter is dedicated to find a similar expression for an air vehicle powered by electric energy with or without energy harvesting systems. This allows to compare whether the addition of energy harvesters improve or worsens the original MAV's design.

The method used in this thesis is based in (Anton, S. R)⁶ [13, 14]. The expression (3.1) is valid for electric powered aircraft in a steady level flight.

$$t_E = \frac{E_B \eta_B}{W_T^{\frac{3}{2}} - P_{harv} \left(\frac{\rho_\infty S C_L^3}{2 C_D^2} \right)^{\frac{1}{2}}} \left(\frac{\rho_\infty S C_L^3}{2 C_D^2} \right)^{\frac{1}{2}} \eta_P \quad (3.1)$$

Where t_E represents the endurance, E_B is the energy from the batteries, W_T is the total weight of the MAV, P_{harv} is the power provided by a harvester, ρ_∞ represents the air density, S stands for the MAV wing surface, C_L and C_D are the lift and drag coefficient respectively, and finally η_B and η_P stand for the efficiency of the batteries and the propulsion system respectively.

3.1 Endurance formulation

The formulation can be derived by considering a basic aerodynamic model to describe the flight of an aircraft as a balance between the energy required for steady, level flight and the energy available from all power sources.

In steady level flight, thrust (T) equals to drag (D) and lift (L) equals to weight (W):

$$T = D \quad (3.2)$$

$$L = W \quad (3.3)$$

The thrust required can be expressed as a function of the weight and the MAV's aerodynamic efficiency by combining both previous equations:

$$T = \frac{W}{L/D} \quad (3.4)$$

Recall that the ratio L/D can be expressed as a ratio of C_L/C_D since:

⁶ The original development of the theory is presented by Thomas et al [21] and cited by Anton, S.R.

$$\frac{L}{D} = \frac{\frac{1}{2}V_{\infty}^2\rho_{\infty}SC_L}{\frac{1}{2}V_{\infty}^2\rho_{\infty}SC_D} = \frac{C_L}{C_D} \quad (3.5)$$

On the other hand the required power for cruise configuration is given by:

$$P_R = T_R V_{\infty} \quad (3.6)$$

Substituting equation (3.4) into (3.6) yields to:

$$P_R = \frac{W}{C_L/C_D} V_{\infty} \quad (3.7)$$

Velocity can be written as well in terms of the weight and lift coefficient by using the relation $L = W = \frac{1}{2}V_{\infty}^2\rho_{\infty}SC_L$. Solving for V_{∞} :

$$V_{\infty} = \sqrt{\frac{2W}{\rho_{\infty}SC_L}} \quad (3.8)$$

Then the power required for steady level flight becomes:

$$P_R = \frac{1}{\eta_P} \frac{W}{C_L/C_D} \sqrt{\frac{2W}{\rho_{\infty}SC_L}} = \frac{1}{\eta_P} \sqrt{\frac{2W^3 C_D^2}{\rho_{\infty}SC_L^3}} \quad (3.9)$$

Note that the term η_P has been added to introduce the efficiency (to convert electric energy into mechanical power) of the aircraft propeller and motor. Other losses may be considered if a careful breakout of this term was made: namely losses due to the speed controller and losses between connections inside the propulsion system. However, when developing the final equation this term will be vanished so the precision does not need to be highly accurate at this stage.

Endurance is introduced using the physics definition of power $P_R = E/t$, where E refers to energy and t refers to time or endurance t_E as it will be called from now on. The energy available in an electric aircraft can be written as a sum of the contribution of the battery power supply plus the extra harvesting devices:

$$E_{avail} = E_B \eta_B + P_{Harv} t_E \quad (3.10)$$

Balance between energy available and the power required for a leveled flight leads to:

$$t_E = \frac{E_{avail}}{P_R} = \frac{E_B \eta_B + P_{Harv} t_E}{W^{3/2}} \left(\frac{\rho_\infty S C_L^3}{2 C_D^2} \right)^{1/2} \eta_P \quad (3.11)$$

Solving for t_E yields to the original expression shown at the beginning of this chapter:

$$t_E = \frac{E_B \eta_B}{W_T^{3/2} - P_{harv} \left(\frac{\rho_\infty S C_L^3}{2 C_D^2} \right)^{1/2}} \left(\frac{\rho_\infty S C_L^3}{2 C_D^2} \right)^{1/2} \eta_P \quad (3.12)$$

3.2 Normalized endurance

When applying expression (3.12) it is useful to compare the results of the endurance of an MAV with the ones obtained in the same vehicle without any kind of harvesters. To do so, the endurance may be expressed as an increment value that can also be normalized with the resulting value from a non-harvesting MAV.

A linear series Taylor expansion of t_E about the point $P_{harv} = 0$ can be used to formulate the normalized change in flight endurance. By taking the aerodynamic terms in (3.12) as a constant:

$$\gamma = \left(\frac{\rho_\infty S C_L^3}{2 C_D^2} \right)^{1/2} \eta_P \quad (3.13)$$

The flight time is expressed as:

$$t_E = E_B \eta_B \left(W_T^{3/2} - P_{harv} \gamma \right)^{-1} \gamma \eta_P \quad (3.14)$$

Now applying the Taylor series expansion for a first order approximation:

$$f(x, y, z) \approx f(x_0, y_0, z_0) + \left. \frac{df}{dx} \right|_{x_0, y_0, z_0} (x - x_0) + \left. \frac{df}{dy} \right|_{x_0, y_0, z_0} (y - y_0) + \left. \frac{df}{dz} \right|_{x_0, y_0, z_0} (z - z_0) \quad (3.15)$$

The endurance can be estimated as:

$$\Delta t_E = t_E - t_E^0 \approx \left. \frac{dt_E}{dE_B \eta_B} \right|_{P_{harv}=0} \Delta E_B \eta_B + \left. \frac{dt_E}{dW_T} \right|_{P_{harv}=0} \Delta W_T + \left. \frac{dt_E}{dP_{harv}} \right|_{P_{harv}=0} \Delta P_{harv} \quad (3.16)$$

$$\Delta t_E \approx \frac{\gamma}{W_T^{3/2}} \Delta E_B \eta_B - \frac{3 E_B \eta_B \gamma}{2 W_T^{5/2}} \Delta W_T + \frac{E_B \eta_B \gamma^2}{W_T^3} \Delta P_{harv} \quad (3.17)$$

Now the normalization is made as explained before with the expression of endurance for a non-harvesting MAV. If $P_{harv} = 0$ is set in equation (3.12):

$$t_E = \frac{E_B \eta_B}{W_T^{3/2}} \gamma \quad (3.18)$$

And dividing expression (3.17) by (3.12) the normalized change in flight time can be written as:

$$\frac{\Delta t_E}{t_E} \approx \frac{\Delta E_B \eta_B}{E_B \eta_B} - \frac{3}{2} \frac{\Delta W_T}{W_T} + \frac{\Delta P_{harv}}{E_B \eta_B / t_E} \quad (3.19)$$

This equation can also be written in terms of changes in mass by decoupling the weight in different terms:

$$W_T = W_B + W_{ST} + W_{harv} \quad (3.20)$$

And using some relations to define the terms in equation (3.19) as well:

$$E_B = e_B m_B \quad (3.21)$$

$$W = mg \quad (3.22)$$

$$P_{harv} = p_{harv} m_{harv} \quad (3.23)$$

$$E_B \eta_B / t_E = p_{ave} m_B \quad (3.24)$$

Where:

- e_B And m_B are specific energy of the battery $\left(\frac{J}{kg}\right)$ and the mass of the battery respectively.
- p_{harv} And m_{harv} is the specific power of the harvester $\left(\frac{W}{kg}\right)$ and the mass of the harvesting system respectively.
- p_{ave} is the specific power supplied by the battery in the non-harvesting design i.e. $p_{ave} = E_B \eta_B / t_E m_B$

Finally the resulting expression is written as:

$$\frac{\Delta t_E}{t_E} \approx \frac{\Delta m_B}{m_B} - \frac{3}{2} \frac{\Delta m_B + \Delta m_{ST} + \Delta m_{harv}}{m_T} + \frac{p_{harv} \Delta m_{Harv}}{p_{ave} m_B} \quad (3.25)$$

where m_T is the total mass of the aerial vehicle. The simple aerodynamic model used in the derivation naturally adds several assumptions about the flight of the aircraft and the ambient environmental conditions, namely imposing constant conditions. The formulation, however, can be used to provide the effects of adding energy harvesting systems to electric powered UAVs and MAVs.

4 Embedded piezoelectric device approach

The embedded piezoelectric beam is a device located inside the structure of the MAV that is meant to vibrate due to the surrounding wind flow over the fuselage. The device will be coupled as a cantilevered beam in order to transmit the vibrations from the structure to the beam. The electromechanical method used to analyze the behavior of a concept device is based in the energy method approach proposed by *duToit* [12]. This chapter will include a developed explanation of this method.

The harvester layout is formed by a bi-morph⁷ cantilevered beam including 4 electrodes and a structural layer and two piezoelectric layers, as shown in figure 4.1:

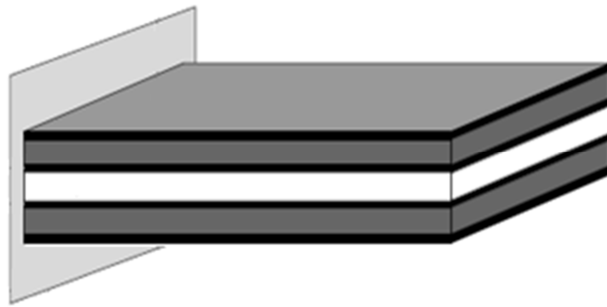


Figure 4.1 Layout of the internal harvester. Black layers represent electrodes, white structural material and grey piezoelectric material

4.1 Piezoelectric constitutive equations

The piezoelectric effect is the combination of the mechanical and electrical behavior of a material. Therefore is imperative to present the mathematical description of such materials in order to develop the electromechanical model for the bending beam approach. On one hand, the Hooke's law relates the mechanical stress (T) and strain (S):

$$S = s T \rightarrow S_{ij} = s_{ijkl} T_{kl} \quad (4.1)$$

Where s_{ijkl} is the compliance or the inverse stiffness.

On the other hand, the expression relating the electric field (E) with the electric displacement (D) is defined as:

$$D = \varepsilon E \rightarrow D_i = \varepsilon_{ij} E_j \quad (4.2)$$

Where ε_{ij} is the electric permittivity

⁷ See annex A for deeper information about Bi-morph configuration and its implications when connecting the electrodes of the different layers.

These two matrix expressions can be combined into coupled equations that adopt the form:

$$S = s T + d^t E \rightarrow S_{ij} = s_{ijkl} T_{kl} + d_{kij} E_k \quad (4.3)$$

$$D = d T + \varepsilon E \rightarrow D_i = d_{ijk} T_{jk} + \varepsilon_{ij} E_j \quad (4.4)$$

These can be written in matrix form as it is shown in expressions (4.5).

$$\begin{aligned} \{S\} &= [s^E]\{T\} + [d^t]\{E\} \\ \{D\} &= [d]\{T\} + [\varepsilon^T]\{E\} \end{aligned} \quad (4.5)$$

This expression is called the (S-D) form of the coupled equations, being S and D the dependent variables. $[d]$ and $[d^t]$ represent the matrix of the direct effect (application of stress to get a voltage output) and converse piezoelectric effect (application of a voltage to induce a stress in the material). The superscript E denotes strain applied at zero or constant electric field and superscript T denotes zero or constant stress.

It is possible to write the same expression in the (T-D) form defining stress and electric displacement as dependent variables:

$$\begin{aligned} \{T\} &= [c^E]\{T\} + [e]\{E\} \\ \{D\} &= [e]\{T\} + [\varepsilon^S]\{E\} \end{aligned} \quad (4.6)$$

Here $[c^E]$ represents the stiffness matrix and $[e]$ is the piezo-electrically induced stress tensor as it relates the stress with to the electric field.

The described model of this project is reduced to the 1D case (bending movement only) and so the equations will be reduced to a simplified expression presented below for both T-D and S-D systems.

$$\begin{Bmatrix} T_3 \\ D_3 \end{Bmatrix} = \begin{bmatrix} c_{33}^E & -e_{33} \\ e_{33} & \varepsilon_{33}^S \end{bmatrix} \begin{Bmatrix} S_3 \\ E_3 \end{Bmatrix} \quad (4.7)$$

$$\begin{Bmatrix} S_3 \\ D_3 \end{Bmatrix} = \begin{bmatrix} s_{33}^E & d_{33} \\ d_{33} & \varepsilon_{33}^T \end{bmatrix} \begin{Bmatrix} S_3 \\ E_3 \end{Bmatrix} \quad (4.8)$$

When applying these equations, the poling direction of the material has to be taken into account because depending on it, the sign of some terms change to be consequent with the reaction on the stress and strain fields. The schematics in figure 4.2 show how a positive and negative poling looks like in a simple three layered section.

The individual energy terms are defined as follows:

$$T_k = \frac{1}{2} \int_{V_S} \rho_S \dot{u}^t \dot{u} dV_S + \frac{1}{2} \int_{V_P} \rho_P \dot{u}^t \dot{u} dV_P \quad (4.12)$$

$$U = \frac{1}{2} \int_{V_S} S^t T dV_S + \frac{1}{2} \int_{V_P} S^t T dV_P \quad (4.13)$$

$$W_e = \frac{1}{2} \int_{V_P} E^t D dV_P \quad (4.14)$$

In both T_k and U there are two contributions due to the structural layer (subscript S) and the piezoelectric layer/s (Subscript P). Electrical energy is only taken into account in piezo-layers and the contribution due to fringing fields in the structure and free space is neglected. The terms u, \dot{u} represent the relative displacement $u(x, t)$ and the successive time derivatives. The rest of the terms (T, D, S, E) are known from the coupled piezoelectric equations.

The term involving the external work is computed with the next expression:

$$\delta W = \sum_{k=1}^{nf} \delta u_k f_k(t) + \sum_{j=1}^{nq} \delta \varphi_j q_j \quad (4.15)$$

It is defined as a combination of two contributions. The first contribution is due to the external forces f_k and mechanical displacements $u(x_k, t)$ on the device counted as discrete forces nf applied at a certain point x_k . The second contribution is due to the electrical potential $\varphi_j = \varphi(x_j, t)$ and a certain amount of charges nq , extracted at discrete electrodes with position x_j

The next step is the substitution of equations (4.12) to (4.14) into (4.11) leading to the developed equation:

$$\int_{t_1}^{t_2} \left[\delta \left(\frac{1}{2} \int_{V_S} \rho_S \dot{u}^t \dot{u} dV_S + \frac{1}{2} \int_{V_P} \rho_P \dot{u}^t \dot{u} dV_P - \frac{1}{2} \int_{V_S} S^t T dV_S - \frac{1}{2} \int_{V_P} S^t T dV_P + \frac{1}{2} \int_{V_P} E^t D dV_P \right) + \sum_{k=1}^{nf} \delta u_k f_k(t) + \sum_{j=1}^{nq} \delta \varphi_j q_j \right] dt = 0 \quad (4.16)$$

The number of variables is reduced using the coupled expressions of the piezoelectric effect. In the definition of the device⁹ the local coordinates are superposed to the global ones, therefore the poling direction chosen in the substitution is the positive alternative, that is, the system provided in expression (4.7).

$$\begin{aligned}
\int_{t_1}^{t_2} \left(\int_{V_S} \rho_S \delta \dot{u}^t \dot{u} dV_S + \int_{V_P} \rho_P \delta \dot{u}^t \dot{u} dV_P - \int_{V_S} \delta S^t c_S S dV_S - \int_{V_P} \delta S^t c^E S dV_P \right. \\
+ \int_{V_P} \delta S^t e^t E dV_P + \int_{V_P} \delta E^t e S dV_P + \int_{V_P} \delta E^t \varepsilon^S E dV_P \\
\left. + \sum_{k=1}^{nf} \delta u_k f_k(t) + \sum_{j=1}^{nq} \delta \varphi_j q_j \right) dt = 0
\end{aligned} \tag{4.17}$$

Please note that (T – D) form has been used in the substitution because then it is easier to continue developing and simplifying the equations.

At this point three assumptions are introduced:

- Rayleigh – Ritz procedure [12]:

The displacement of a structure is written as the sum of nr individual mode shapes ($\psi_{ri}(x)$), multiplied by a generalized mechanical coordinate $r_i(t)$. Since only bending movement is considered the only displacement allowed is on Z axis along the longitudinal direction:

$$u(x, t) = z(x_a, t) = \sum_{i=1}^{nr} \psi_{ri}(x_a) r_i(t) = \psi_r(x_a) r(t) \tag{4.18}$$

- Euler Bernoulli beam theory [12]:

Allows the axial strain in the beam to be written in terms of the beam neutral axis displacement and the distance from neutral axis as:

$$S(x, t) = -x_t \frac{\delta^2 z(x_a, t)}{\delta x_a^2} = -x_t \psi_r'' r(t) \tag{4.19}$$

- Constant electric field across the piezoelectric [12]:

Although the constant nature of the electric field considered in the device, the electric potential for each of the nq electrode pairs can be written in terms of a potential distribution ψ_{vj} and the generalized electrical coordinate $v_j(t)$

⁹ Refer to figures 4.1 and 4.2

$$\varphi(x, t) = \sum_{j=1}^{nq} \psi_{v_j}(t) v_j(t) = \psi_v v(t) \quad (4.20)$$

Note that prime signs on ψ_r denote derivative with respect to the axial position x_a .

The substitution of these definitions into the main equation (4.17) yields to:

$$\begin{aligned} \int_{t1}^{t2} \left(\int_{V_S} \rho_s \delta r^t \psi_r^t \psi_r \dot{r} dV_S + \int_{V_P} \rho_p \delta r^t \psi_r^t \psi_r \dot{r} dV_P - \int_{V_S} \delta r^t (-x_t \psi_r'')^t c_s (-x_t \psi_r'') r dV_S \right. \\ \left. - \int_{V_P} \delta r^t (-x_t \psi_r'')^t c^E (-x_t \psi_r'') r dV_P + \int_{V_P} \delta r^t (-x_t \psi_r'')^t e^t (-\nabla \psi_v) v dV_P \right. \\ \left. + \int_{V_P} \delta v^t (-\nabla \psi_v)^t e (-x_t \psi_r'') r dV_P + \int_{V_P} \delta v^t (-\nabla \psi_v)^t \varepsilon^S (-\nabla \psi_v)^t v dV_P \right. \\ \left. + \sum_{k=1}^{nf} \delta r_k^t \psi_{r,k}^t f_k + \sum_{j=1}^{nq} \delta v_j^t \psi_{v,j}^t q_j \right) dt = 0 \end{aligned} \quad (4.21)$$

Using integration by parts and grouping terms by factors δr^t and δv^t two governing equations are obtained:

$$\begin{aligned} - \int_{V_S} \psi_r^t \rho_s \varphi_r \ddot{r} dV_S - \int_{V_P} \psi_r^t \rho_p \varphi_r \ddot{r} dV_P - \int_{V_S} (-x_t \psi_r'')^t c_s (-x_t \psi_r'') r dV_S \\ - \int_{V_P} (-x_t \psi_r'')^t c^E (-x_t \psi_r'') r dV_P + \int_{V_P} (-\nabla \psi_v)^t e (-x_t \psi_r'') r dV_P \\ + \sum_{i=1}^{nf} \varphi_{r,k}^t f_k = 0 \end{aligned} \quad (4.22)$$

$$\int_{V_P} (-x_t \psi_r'')^t e^t (-\nabla \psi_v) v dV_P + \int_{V_P} (-\nabla \psi_v)^t \varepsilon^S (-\nabla \psi_v)^t v dV_P + \sum_{j=1}^{nq} \psi_{v,j} q_j = 0 \quad (4.23)$$

Each of these terms is defined as mass (M) stiffness (K), coupling (Θ) and capacitive (C_p) matrices as showed in the following equations:

$$M = \int_{V_S} \psi_r^t \rho_s \varphi_r \ddot{r} dV_S + \int_{V_P} \psi_r^t \rho_p \varphi_r \ddot{r} dV_P \quad (4.24)$$

$$K = \int_{V_S} (-x_t \psi_r'')^t c_s (-x_t \psi_r'') r dV_S - \int_{V_P} (-x_t \psi_r'')^t c^E (-x_t \psi_r'') r dV_P \quad (4.25)$$

$$\Theta = \int_{V_P} (-\nabla\psi_v)^t e (-x_t\psi_r'')r dV_P \quad (4.26)$$

$$C_P = \int_{V_P} (-\nabla\psi_v)^t \varepsilon^S (-\nabla\psi_v)^t v dV_P \quad (4.27)$$

The final governing equations are:

$$M\ddot{r} + Kr - \Theta v = \sum_{i=1}^{nf} \varphi_r^t(x_k) f_k(t) \quad (4.28)$$

$$\Theta^t r + C_P v = - \sum_{j=1}^{nq} \psi_{v,j}(x_j) q_j(t) \quad (4.29)$$

A base excitation will be the input when applying these equations. To represent the beam's inertial load from this excitation, the structure is discretized into n elements of length x_a and the local inertial load is applied on the k^{th} element, or $f_k = m_k \Delta x_a \ddot{w}_B$. This results in nf discrete loads. m_k is the element mass per length. The loading is summed for all the elements. In the limit of $\Delta x_a \rightarrow dx_a$, the summation reduces to the integral over the structure length and a mass per length distribution is used, $m(x_a)$. For simplicity, it has been assumed here that the beam cross-section is uniform in the axial direction so that $m(x_a) = m = constant$. The forcing vector on the right side of expression (4.28) is then defined as B_f :

$$B_f = \int_0^L m(x_a) \varphi_r^t dx_a = m \int_0^L \varphi_r^t dx_a \quad (4.30)$$

Mechanical damping is added through the addition of a viscous damping term, \mathbf{C} , to equation (4.28) to obtain (4.31). When multiple bending modes are investigated, a proportional damping scheme is often used to ensure uncoupling of the equations during the modal analysis.

The right hand side of eq. (4.29) reduces to a column vector, q of length nq (the number of electrode pairs) with element values q_T ($q_T = \sum_{j=1}^{nq} q_j$). This equation can be differentiated with respect to time to obtain current. The current can be related to the voltage, assuming that the electrical loading is purely resistive, R_l since $v = iR = \frac{dq}{dt}$.

After substituting in both governing equations one get:

$$M\ddot{r} + C\dot{r} + Kr - \Theta v = B_f \ddot{w}_B \quad (4.31)$$

$$\Theta^t r + C_p v + q = 0 \quad (4.32)$$

4.2.2 Modal analysis: Simple bending beam

The previous section has shown that governing equations for a piezoelectric beam can be written in terms of the mechanical displacement assuming a function φ_r that describes the shape of the beam and it is a valid solution to the mentioned equations as well.

Dynamic Euler-Bernoulli beam theory is used to find the modal solution. [12]

$$\frac{d^2}{dx^2} \left((cI)_e \frac{d^2 u}{dx^2} \right) = -m \frac{d^2 u}{dt^2} + q(x) \quad (4.33)$$

Remember that stiffness $(cI)_e$ is considered constant because the beam is homogeneous along the x-axis.

In the absence of a transverse load, $q(x)$, the free vibration equation is obtained. This equation can be solved using a Fourier decomposition of the displacement into the sum of harmonic vibrations of the form

$$u(x, t) = \psi_r(x_a) r(t) = \text{Re}[\varphi(x) e^{-i\omega t}] \quad (4.34)$$

Where ω , is the vibration frequency. Then for each value of the frequency, an ordinary differential equation can be solved:

$$(cI)_e \psi_{rN}^{IV} - m\omega_N^2 \varphi_{rN} \quad (4.35)$$

Please note that the equation (4.33) has been modified into expression (4.35) to include the term of natural frequency ω_N in order to find the different mode shapes of the beam. N Refer to a generic mode shape.

And the general solution for the above equation (4.35) is:

$$\varphi_{rN} = A_1 \sinh(\lambda_N x_a) + A_2 \cosh(\lambda_N x_a) + A_3 \sin(\lambda_N x_a) + A_4 \cos(\lambda_N x_a) \quad (4.36)$$

Where $\left(\frac{\lambda_N}{L}\right)^2 = \frac{m\omega^2}{(cI)_e}$ is a parameter defined for convenience due to the form of expression (4.35).

A_1, A_2, A_3, A_4 are constants solved by applying the boundary conditions to a particular case. The proposed device is a cantilevered beam without any external force applied on the structure. Thus the boundary conditions are:

- No displacement nor rotation at fixed end

$$(\varphi_{rN})_{x=0} = 0 \quad \left(\frac{d\varphi_{rN}}{dx}\right)_{x=0} = 0 \quad (4.37)$$

- Null moment and shear force at the free end

$$\left(\frac{d^2\varphi_{rN}}{dx^2}\right)_{x=L} = 0 \quad \left(\frac{d^3\varphi_{rN}}{dx^3}\right)_{x=L} = 0 \quad (4.38)$$

The solution of these constants is unique for a set of boundary conditions but the displacement depend on the frequency which at the same time define the mode shape of the beam.

Solving the system to determine the constants leads to the well-known transcendental expression:

$$\cosh(\lambda_N L) \cos(\lambda_N L) + 1 = 0 \quad (4.39)$$

Thus by using numerical methods, the mode shapes φ_N and the natural frequencies ω_N are found:

$$\varphi_{nr} = K \left[\cosh(\lambda_N x) - \cos(\lambda_N x) + \frac{(\cosh(\lambda_N L) + \cos(\lambda_N L)) \cdot (\sin(\lambda_N x) - \sinh(\lambda_N x))}{\sin(\lambda_N L) - \sinh(\lambda_N L)} \right] \quad (4.40)$$

Where: $\omega_N = \lambda_N \sqrt{\frac{(cI)_e}{m}}$ and K is an arbitrary constant defining an upper value of the tip displacement.

A fixed value of this constant is not possible to establish so the criterion in this case will be to consider a maximum value set at $\varphi_{nr}(L) = 2$

Next step is find the values of M, K, θ, C_p and B_f expressed in eq. (4.24) to (4.27).

At this point, voltage (v), intensity (I), tip displacement (r) and power (P_{out}) are the output variables that will be used to design the optimal piezoelectric device after solving the governing equations of the previous section. To do it, the following assumptions have been considered so this way the governing equations can be reduced to a scalar form.

- $\varphi_{rn} = \varphi_{r1}$ only the first bending mode is taken into account
- Only one electrode pair

The governing equations form a second order system and for this reason they can be written as follows:

$$\ddot{r} + 2\xi_m\omega_1\dot{r} + \frac{\theta}{Mv} = -B_f \frac{\ddot{w}_B}{M} \quad (4.41)$$

$$\theta\dot{r} + C_p\dot{v} + \frac{1}{R_l}v = 0 \quad (4.42)$$

where the factors $\alpha = \omega_1 R_l C_p$, $\kappa^2 = \frac{\theta^2}{K C_p}$ and $\Omega = \frac{\omega}{\omega_1}$ have been defined for convenience:

- α is a dimensionless time constant.
- κ^2 is a structure/system electromechanical coupling coefficient
- Ω is the ratio between the excitation ω and the first mode frequency ω_1

Using Laplace transforms, the governing equations can be evaluated and the output magnitudes can be determined:

$$\left| \frac{r}{B_f \ddot{w}_B} \right| = \frac{1}{K} \frac{\sqrt{1 + (\alpha\Omega)^2}}{\sqrt{[1 - (1 + 2\xi_m\alpha)\Omega^2]^2 + [(2\xi_m + \{1 + \kappa^2\}\alpha)\Omega - \alpha\Omega^3]^2}} \quad (4.43)$$

$$\left| \frac{v}{B_f \ddot{w}_B} \right| = \frac{1}{|\theta|} \frac{\alpha\kappa^2\Omega}{\sqrt{[1 - (1 + 2\xi_m\alpha)\Omega^2]^2 + [(2\xi_m + \{1 + \kappa^2\}\alpha)\Omega - \alpha\Omega^3]^2}} \quad (4.44)$$

$$\left| \frac{P_{out}}{B_f \ddot{w}_B} \right| = \frac{\omega_1}{K} \frac{\alpha\kappa^2\Omega^2}{[1 - (1 + 2\xi_m\alpha)\Omega^2]^2 + [(2\xi_m + \{1 + \kappa^2\}\alpha)\Omega - \alpha\Omega^3]^2} \quad (4.45)$$

4.2.3 Modal analysis: Bending beam adding a tip mass

The solving procedure of the electromechanical model for a bending beam with a tip mass is analogous to that shown in subsection 4.2.2. But in this case the boundary conditions will be modified to suit the new configuration. This case is more general than the simple bending beam so it has been assumed that the gravity center of the tip mass does not match the same horizontal plane as the piezoelectric structure. For the same reason, the boundary conditions will be reduced to the ones of the simple cantilever beam if a mass tip $m_{tip} = 0$ is set in the solver. The pictures in figure 4.3 give the general layout of the device configuration.

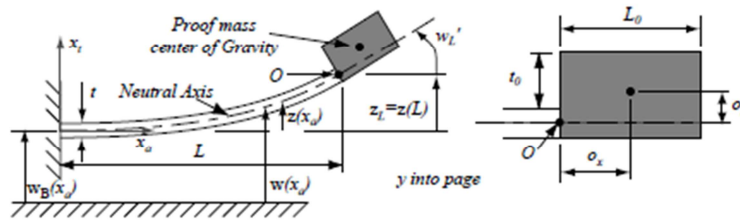


Figure 4.3 Layout of the bending beam with added tip mass¹⁰. Image extracted from [12]

The boundary conditions for this configuration are expressed:

- At the fixed end:

$$(\varphi_{rN})_{x=0} = 0 \quad \left(\frac{d\varphi_{rN}}{dx}\right)_{x=0} = 0 \quad (4.46)$$

- At the point where the beam and the tip mass are connected:

$$(cI)_e z_L'' \omega_N^2 J_0 z_L' - \omega_N^2 S_0 z_L = 0 \quad (4.47)$$

$$(cI)_e z_L''' \omega_N^2 M_0 z_L - \omega_N^2 S_0 z_L' = 0 \quad (4.48)$$

Where: $M_0 = m_0 L_0$, $S_0 = M_0 o_x$, $J_0 = J_{yy} + M_0(o_x^2 + o_z^2)$ and J_{yy} is the mass moment of inertia of the proof mass around its center of gravity.

Beyond this point, the procedure is equal to that of the simple clamped beam, but the results are slightly different. The first couple of boundary conditions determine that the constants of the general solution eq. (4.36) are related: $A_1 = -A_3 = K_1$ and $A_2 = -A_4 = K_2$ so when solving the system only two constants (K_1, K_2) need to be taken into account.

The rest of the of the boundary conditions lead to the system:

¹⁰ The units of the image are consistent with the ones exposed in this thesis

$$\begin{bmatrix} A_{11} & A_{12} \\ A_{21} & A_{22} \end{bmatrix} \begin{bmatrix} K_1 \\ K_2 \end{bmatrix} = 0 \quad (4.49)$$

$$A_{11} = (\sinh \bar{\lambda}_N + \sin \lambda_N) + \lambda_N^3 \bar{J}_0(-\cosh \lambda_N + \cos \lambda_N) + \lambda_N^2 \bar{S}_0(-\sinh \bar{\lambda}_N + \sin \lambda_N) \quad (4.50)$$

$$A_{12} = (\cosh \lambda_N + \cos \lambda_N) + \lambda_N^3 \bar{J}_0(-\sinh \bar{\lambda}_N - \sin \lambda_N) + \lambda_N^2 \bar{S}_0(-\cosh \lambda_N + \cos \lambda_N) \quad (4.51)$$

$$A_{21} = (\cosh \lambda_N + \cos \lambda_N) + \lambda_N \bar{M}_0(\sinh \bar{\lambda}_N - \sin \lambda_N) + \lambda_N^2 \bar{S}_0(\cosh \lambda_N - \cos \lambda_N) \quad (4.52)$$

$$A_{22} = (\sinh \bar{\lambda}_N - \sin \lambda_N) + \lambda_N \bar{M}_0(\cosh \lambda_N - \cos \lambda_N) + \lambda_N^2 \bar{S}_0(\sinh \bar{\lambda}_N + \sin \lambda_N) \quad (4.53)$$

The resonance frequencies for each mode are obtained by solving for $\bar{\lambda}_N$ such that the determinant equals zero. Successive values of $\bar{\lambda}_N$ correspond again to the beam modes and the natural

frequency of each mode can be determined with $\omega_N^2 = \bar{\lambda}_N^2 \sqrt{\frac{(cl)_e}{mL^4}}$

Then the general solution is expressed in terms of a single arbitrary constant K :

$$\varphi_{Nr} = K \left[\cosh(\lambda_N x) - \cos(\lambda_N x) + \frac{A_{12}}{A_{11}} (\sin(\lambda_N x) - \sinh(\lambda_N x)) \right] \quad (4.54)$$

The effective mass M of the structure obtained from the Lagrange equations of motion given in equation (4.24) is now replaced for the more general expression:

$$M = \int_{V_S} \psi_r^t \rho_s \varphi_r dV_s + \int_{V_P} \psi_r^t \rho_p \varphi_r dV_p + M_0 (\varphi_r(L))^t \varphi_r(L) + 2S_0 (\varphi_r(L))^t \varphi_r(L) + I_0 (\varphi_r'(L))^t \varphi_r'(L) \quad (4.55)$$

Lastly, the external work term needs to be re-evaluated to include the inertial loading due to the proof mass at the beam tip. In eq. (4.30) the forcing vector, B_f was defined to account for the inertial loading due to a base excitation. It was previously assumed (for simplicity) that the device is of uniform cross-section in the axial direction. However, the device now consists of two distinct sections, the uniform beam and uniform proof mass. Both sections contribute to the inertial loading of the device. The proof mass displacement is calculated in terms of the displacement and rotation of the tip of the beam. The forcing function definition is extended to account for the proof mass by including two additional terms in the forcing vector:

$$B_f = m \int_0^L (\varphi_r(x_a))^t dx_a + m_0 (\varphi_r(L))^t \int_L^{L+L_0} dx_a + m_0 (\varphi_r'(L))^t \int_L^{L+L_0} x_a dx_a \quad (4.56)$$

The output values are obtained again using the solution of the governing equations. Expressions from (4.43) to (4.45) remain exactly the same for the case of the tip mass addition:

$$\left| \frac{r}{B_f \ddot{w}_B} \right| = \frac{1}{K} \frac{\sqrt{1 + (\alpha\Omega)^2}}{\sqrt{[1 - (1 + 2\xi_m\alpha)\Omega^2]^2 + [(2\xi_m + \{1 + \kappa^2\}\alpha)\Omega - \alpha\Omega^3]^2}} \quad (4.57)$$

$$\left| \frac{v}{B_f \ddot{w}_B} \right| = \frac{1}{|\theta|} \frac{\alpha\kappa^2\Omega}{\sqrt{[1 - (1 + 2\xi_m\alpha)\Omega^2]^2 + [(2\xi_m + \{1 + \kappa^2\}\alpha)\Omega - \alpha\Omega^3]^2}} \quad (4.58)$$

$$\left| \frac{P_{out}}{B_f \ddot{w}_B} \right| = \frac{\omega_1}{K} \frac{\alpha\kappa^2\Omega^2}{[1 - (1 + 2\xi_m\alpha)\Omega^2]^2 + [(2\xi_m + \{1 + \kappa^2\}\alpha)\Omega - \alpha\Omega^3]^2} \quad (4.59)$$

Those are the output values taken into account when gathering information to present the results of the thesis.

5 Results

This section show the results obtained for the cantilevered device under MAVs approximate conditions of air stream over a lifting surface. A scaled wing section was used to perform a simulation to evaluate the evolution of the aerodynamic coefficients and extract values of base excitation to use them later in the code based on the electro-mechanical model seen on section 4.2.

5.1 Accelerations on the MAV

Getting current data of vibrations in MAVs is quite a difficult task. The flow around the vehicle is not easy to model and existing information on actual MAV projects is not available. In this thesis, a model performed by *Duarte da Câmara* [15] using detached eddy simulations (DES) has been used to extract values of fluctuations on C_L and C_D over a wing with sinusoidal leading edge. The parameters defining the wing surface and stream conditions are listed in table5.1.

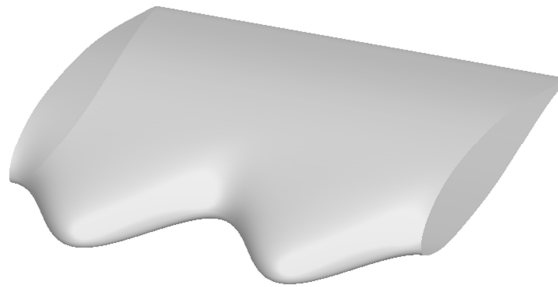


Figure 5.1 Layout of the wing surface used to extract fluctuations of C_L and C_D

Parameter	Value	Unit
Chord (c)	0.25	m
Aspect ratio (Δ)	1	-
Air speed (v)	9.35	m/s
Air density (ρ)	1.22	kg/m^3
Angle of attack	22	$^\circ$

Table 5.1 Parameters of the lifting surface

A 45 seconds simulation with the presented configuration was performed and the results of aerodynamic coefficients as well as frequency of the largest vortex are presented in figures 5.2 and 5.3, respectively.

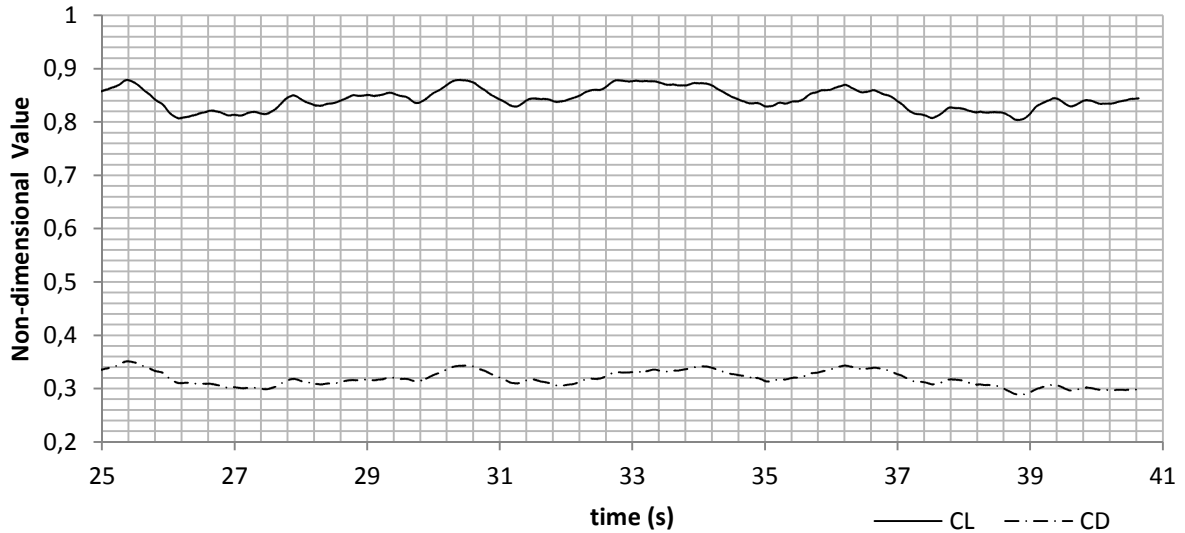


Figure 5.2 Simulation, C_L and C_D with respect to time

Note that the graphic only plots values from $t = 25s$, to avoid transitory state.

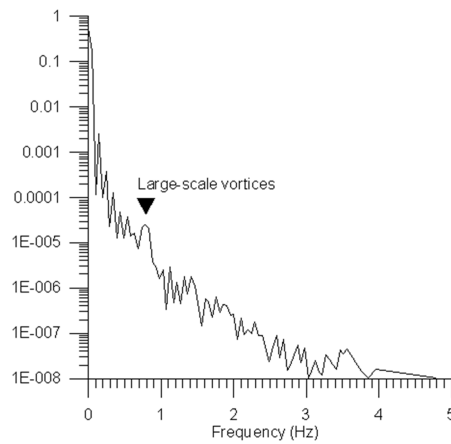


Figure 5.3 Simulation frequency spectrum

Higher amplitudes than the value pointed by the mark suggest that there is noise, and frequency values much higher than 1 Hz do not show significant amplitude. The values of amplitude are normalized so the maximum value is 1.

With these plots and the parameters of the simulation, a base acceleration can be deduced to estimate the excitation and perform simulations of the cantilever beam. Lift and drag are obtained from their relation with C_L and C_D :

$$L(t) = \frac{1}{2} C_L(t) \rho_{air} v^2 \Delta c^2 \quad (5.1)$$

$$D(t) = \frac{1}{2} C_D(t) \rho_{air} v^2 \Delta c^2 \quad (5.2)$$

And the total force applied on the wing is computed with the known expression:

$$F_{total}(t) = \sqrt{L(t)^2 + D(t)^2} \quad (5.3)$$

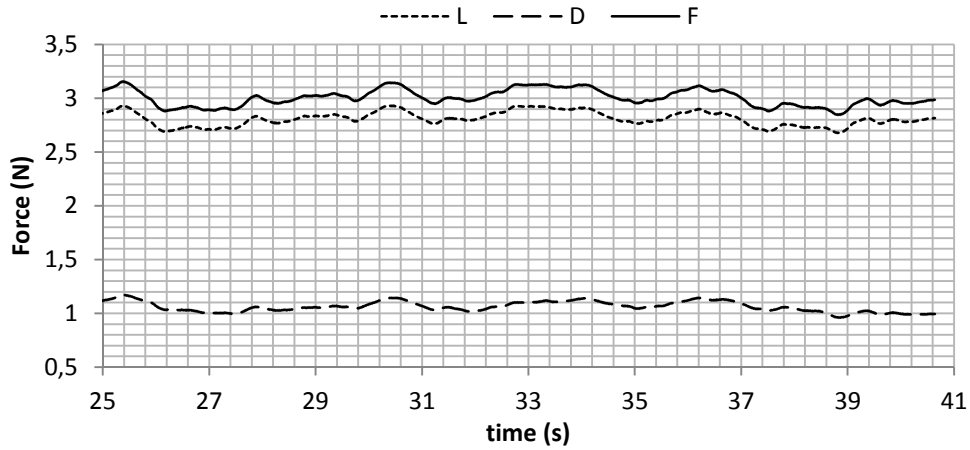


Figure 5.4 Simulation outputs, lift, drag and total force

Using RMS¹¹ of the data in figure 5.4 to calculate the amplitude of total aerodynamic force oscillations leads to:

$$F_{RMS} = 0,076642 \text{ N} \quad (5.4)$$

$$F_{mean} = 3,004265 \text{ N} \quad (5.5)$$

Since the target GTOW of a typical MAV is approximately 100g and taking in consideration that the lifting surface tested is considerably bigger (25 cm and an estimated weight of 400 g) than the expected for a vehicle of this kind (15 cm), the base acceleration can be bounded to values inside the following range:

$$a_{base} = \frac{F_{RMS}}{m_{MAV}} \rightarrow 100 \leq m_{MAV} \leq 400 \text{ [g]} \quad (5.6)$$

$$0,2 \leq a_{base} \leq 0,77 \text{ [m/s}^2\text{]} \quad (5.7)$$

5.2 Material selection

In view of the results showed in section 5.1 it is clear that the material been sought needs to respond under very low base accelerations but also at very low frequencies. In order to choose the best candidate among all the PZTs found in the literature, a selection process has been made.

¹¹ Root-mean square

The process consists on simulating a device with a standard geometry and fixed base acceleration, changing only the material. Then for each material the base excitation is forced to actuate in a range of frequencies and the electric circuit is studied for several load resistances. This method allows the identification of the resonance frequency f_r of the beam and the load resistance R_l that optimizes the output results. There is another interesting frequency that shows a peak in the produced power: the anti-resonance frequency f_{ar} , the natural frequency of the device under open circuit conditions. The resistance load that maximizes the power at this frequency is called $R_{l_{oc}}$ ¹². Similarly, the f_r is the natural frequency associated to the device when short circuit conditions are applied. The optimal load resistance is called $R_{l_{sc}}$ (sc, referring to short-circuit).

Apart from the piezoelectric material, the harvester contains the structural layer which influences its behavior. The constitutive equations show that power is proportional to the density to the power of 1.5 ($P \propto \rho^{\frac{3}{2}}$) and inversely proportional to the Young modulus ($P \propto \frac{1}{C_{E_{xx}}}$). The ideal structural material should be heavy and very flexible at the same time, properties usually not found together. Aluminum has been the first option to fit the requirements because it is a metal with a slightly low Young modulus and even though its density is also low compared to the ones of the PTZs it is high enough to maintain an effective density ρ_{eff} inside the margins of the study. Aluminum will suit well the needs of the project at this stage of the design, then when the final device is under consideration the structural layer might be changed for a better option. An important remark is that aluminum conducts electricity so the structural layer should be treated with an insulating material to avoid undesired short circuits. The initial conditions used to make the first test are listed in table 5.2. The thickness data selected represent commercialized thicknesses of piezoelectric plates. Length and width correspond to values taken in previous simulations [12] to confirm the reliability of future results of this thesis. Figure 5.5 shows the layout of the harvester.

a	0.77	m/s^2
L	55	mm
W	31,8	mm
t_s	0,14	mm
t_p	0,27	mm
t_{total}	0,68	mm
ρ_s	2700	kg/m^3
ρ_p	-	kg/m^3
ρ_{eff}	-	kg/m^3
m	-	g

Table 5.2 Parameters of the piezoelectric material test. Last three parameters vary with the chosen material

¹² Open circuit load resistance

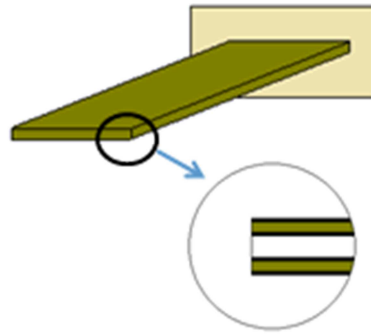


Figure 5.5 Layout of the harvester for material testing. White layer represent structural material and green represents piezoelectric material

Where:

- L represent the length of the harvester
- W represent the width of the harvester
- A stands for the area of the harvester,
- t represent the thickness. The sub index s , p and $total$ define the piezoelectric and the structure layer and total thickness respectively.
- m mass of the harvester

Figures 5.6 and 5.7 compare 5 types of PZT that were pre-selected from a larger list (see bibliographical sources [8] [9] [10] [11]). Power vs. frequency is plotted at the corresponding R_l of each material and for both cases: open and short circuit.

First thing that can be observed from the figures is that PZT 7A is excited at quite higher frequencies than the rest of the materials. PZT 5A is also excited at higher frequencies but not as separated as 7A but in any case both of them present lower power peaks compared with the rest of the candidates. The two best candidates are PZT 5J and PZT 4D both show similar power outputs and the natural frequencies does not exceed the 190 Hz although these values are significantly high for the proposal of the thesis.

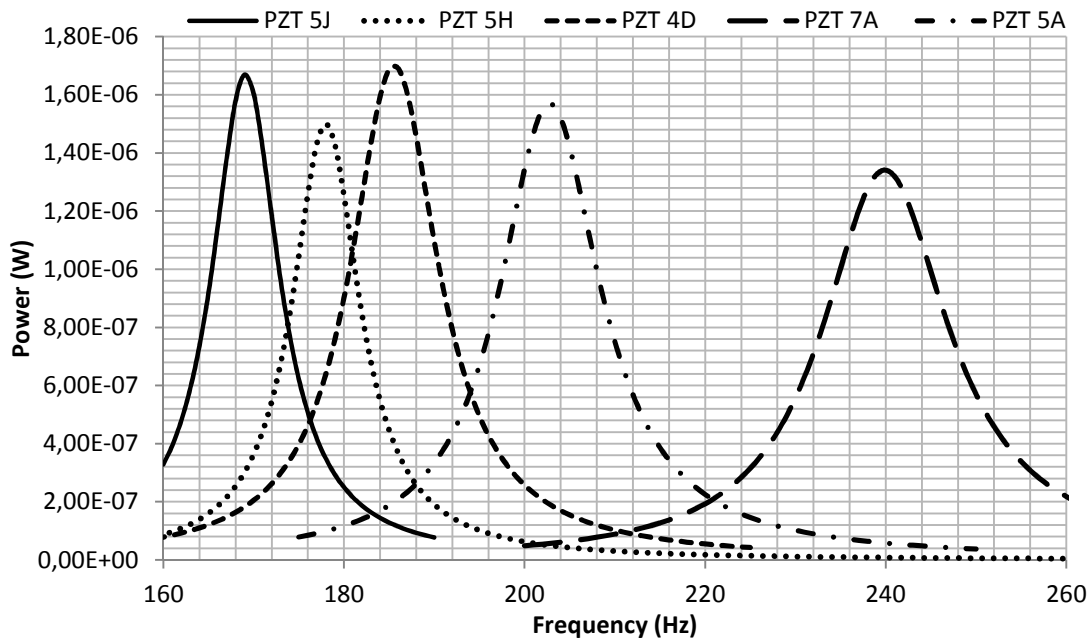


Figure 5.6 Power vs. frequency at $R_{l_{sc}}$ for each material, short circuit case.

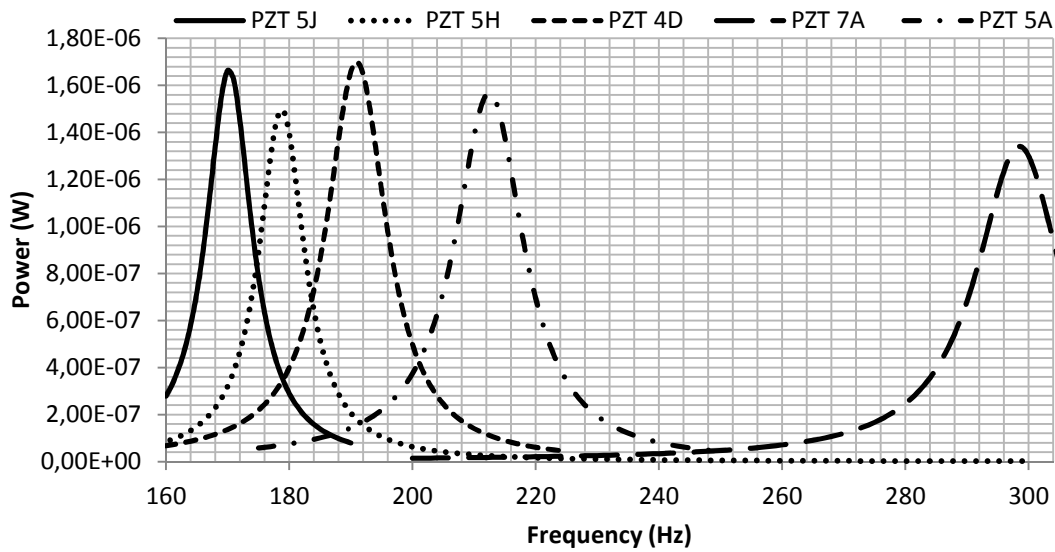


Figure 5.7 Power vs. frequency at $R_{l_{oc}}$ for each material, open circuit case.

A final point to be taken into account is the difference between the f_r and f_{ar} , the more similar the frequencies the easier to achieve lower values for both modes altering the geometry like adding a tip mass. Comparing both materials the conclusion is that PZT 5J is slightly better, as shown in figure 5.8.

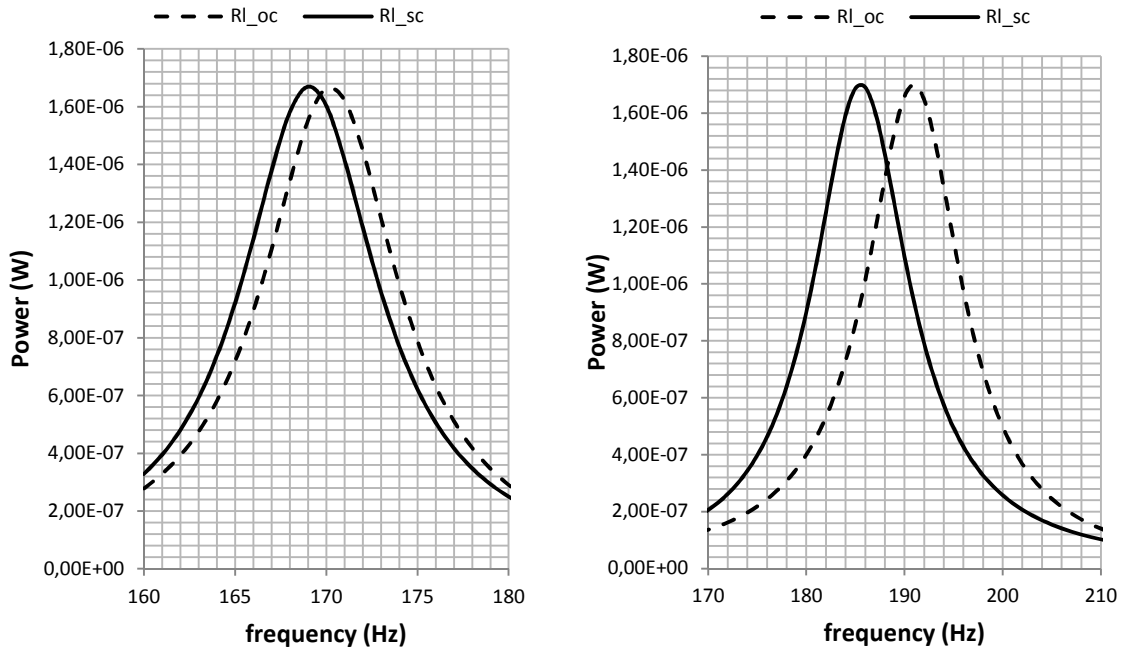


Figure 5.8 Comparison of natural frequencies for PZT 5J (left) and PZT 4D (right)

Even though the peak of power is higher for PZT 4D reduce the frequency is a more important issue because the power difference is very low, recall that the output is $\propto 10^{-6}$ [W]. A minor observation related to the power levels is that for the rest of the swept frequencies the values are higher for PZT 5J.

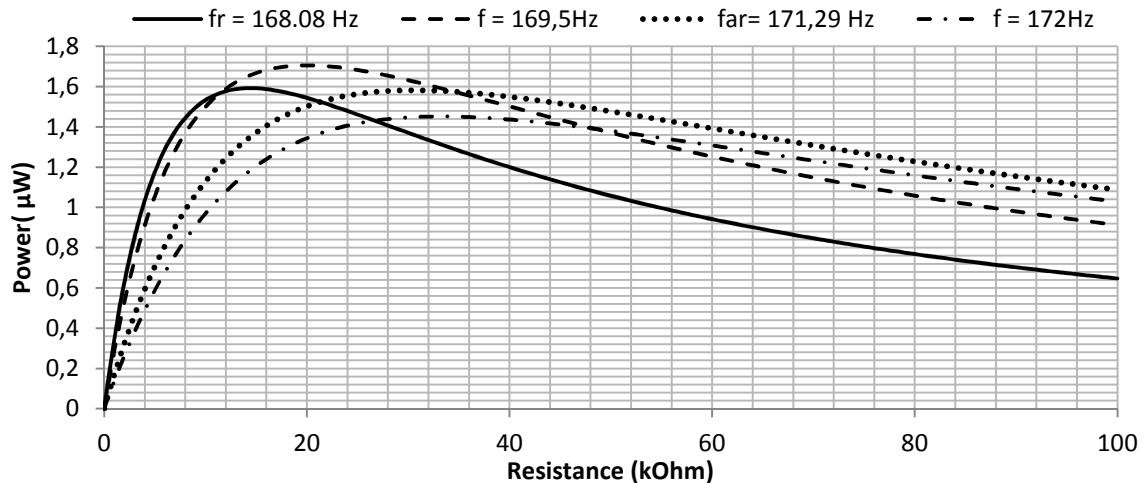


Figure 5.9 Power vs. resistive load varying the frequency of excitation

It may be difficult to find the exact resistive load to build the electrical circuit that contains the harvester or adjust the value considering the other elements of the circuits, for this reason the behavior at f_r and f_{ar} vs. R_l is studied to see how it affects to the power and voltage outputs, as seen in figure 5.9.

Performing these plots an interesting feature is found that could have been overlooked only using the optimal resistive loads given by the software. Another value f between the resonance and anti-resonance frequency allows reaching higher power outputs (at a certain resistive load range). This happens due to the fact that optimization expressions have been simplified with some assumptions which make the results less accurate as well as missing some important features of the coupled response (mainly anti-resonance). Figure 5.10 shows a complete sweep of the frequencies along a resistive load range used to find the exact point where the power reaches the true maximum value.

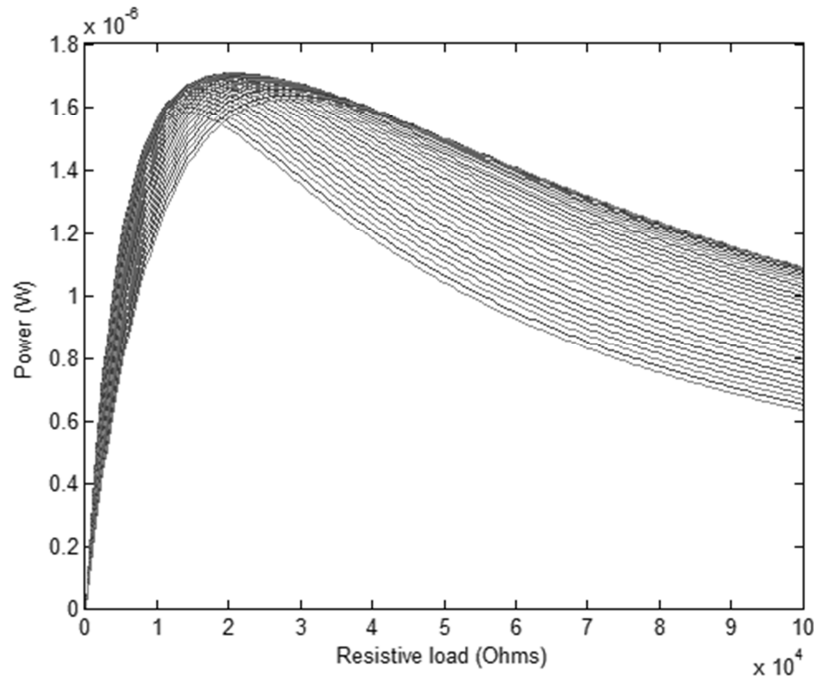


Figure 5.10 Accurate swept of frequencies vs. resistive loads

Extracting out the values shows:

$$P_{max} = 1,7065 \cdot 10^{-6} W \quad (5.8)$$

$$f_{P_{max}} = 169,7 \text{ Hz} \quad (5.9)$$

$$R_{l_{P_{max}}} = 21000 \Omega \quad (5.10)$$

Those results are not definitive but they warn about a possible underestimation of the capabilities of the material being used. Note that there is an increasing of 4.3% with respect to the maximum values at f_r and f_{ar} .

After the whole study of the plots, PZT 5J is the candidate to design the harvester. It is worth to mention that materials can be doped improving their qualities, but since the aim of the project is to find a determined application to piezoelectric harvesters the deeper study of the materials has not been investigated.

5.3 Geometry adjustment

The dimensions of the piezoelectric beam must fit on the interior of the MAV. Maximum dimensions are critical since longer beams produce better results, but then again are difficult to embed them inside the vehicle. For the sake of the project dimensions will be chosen to take the maximum benefit of the piezoelectric effect leaving in a second plane how to adjust the device into the MAV.

Device geometry will never surpass 5% of the total area of the MAV taking as a reference the goal requirements of the MAVs presented in the section 2 where the maximum dimension should be inferior to 15 cm ,the area of the harvester is set at:

$$A_{MAV_{max}} = 225 \text{ cm}^2 \rightarrow A_{harv_{max}} = 0,05 \cdot A_{MAV_{max}} = 11,25 \text{ cm}^2 \quad (5.11)$$

In order to find the optimal dimensions, length L and width W were set in different values changing the shape of the harvester without interfering on the area. The 9 variations of the device are listed in table 5.3.

Parameter	G1	G2	G3	G4	G5	G6	G7	G8	G9	Units
A	11,25	11,25	11,25	11,25	11,25	11,25	11,25	11,25	11,25	cm^2
L	112,50	90,00	75,00	64,29	56,25	50,00	45,00	40,91	37,50	mm
W	10	12,5	15	17,5	20	22,5	25	27,5	30	mm
t_s	0,14	0,14	0,14	0,14	0,14	0,14	0,14	0,14	0,14	mm
t_p	0,27	0,27	0,27	0,27	0,27	0,27	0,27	0,27	0,27	mm
t_{total}	0,68	0,68	0,68	0,68	0,68	0,68	0,68	0,68	0,68	mm

Table 5.3 Geometric dimensions for different harvesters

The thickness has been kept equal for the different geometries (Gx) because does not influence the results in a great amount. Another reason is that these layer thicknesses have been tested in previous experiments so their manufacturing is possible.

Each of the previous geometry layouts have been tested for several frequencies and resistance loads similarly to what have been done in the previous section. These tests allow understanding how the power changes with dimensions and gives a notion of the order of magnitude that can be achieved. Figure 5.11 shows the maximum power vs. frequency for the previous geometries.

Note how the optimal frequency is radically reduced but the effect is lost quickly by reducing the length of the beam. The power is also affected in the same way; actually the shape of the graphic shows an exponential behavior in both the frequency and the power. The figure is linked with table 5.4 showing other key parameters such as the voltage the numerical value of the maximum power and the power density of the harvester. The last one is crucial to implement the endurance test and prove the viability of installing the device in MAVs.

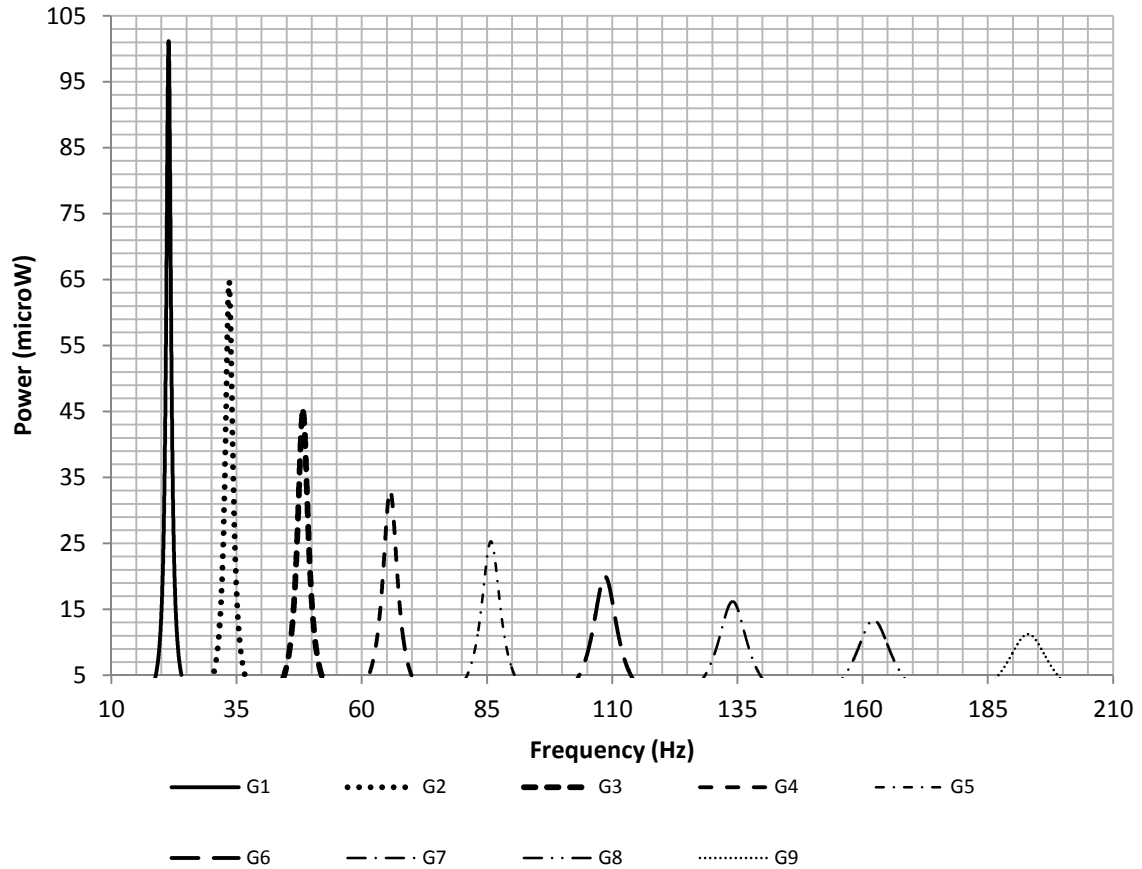


Figure 5.11 Power vs. frequency for nine different devices

	V_{max} (V)	$Power_{max}$ (μW)	$Power\ density$ ($\frac{mW}{kg}$)
G1	3,80098	101,70	19,9294
G2	2,450077	64,76	12,6898
G3	1,710268	44,97	8,8123
G4	1,249821	33,05	6,4757
G5	0,958238	25,30	4,9569
G6	0,757371	19,99	3,9166
G7	0,61351	16,19	3,1724
G8	0,506854	13,38	2,6220
G9	0,425972	11,24	2,2031

Table 5.4 Output results for the different harvesters

Clearly the best configuration is G1 and in general will always be the one with the largest length value. The center of gravity CG is moving away from the root so the bending moment gets higher and increase the stress applied in the piezoelectric layer. For a realistic design the ratio $\frac{Length}{width}$ or aspect ratio, cannot be undefinably large for the same reasons why the maximum area is bounded to a 5 % of the total plane area of the MAV.

G1 length is considerably long but it is taken as the model to add a tip mass and improve even more the power produced by the harvester. Then it is compared with the endurance studies and if it is possible, the geometry is adjusted to the optimal shape. Comparing the power density of the batteries (see section 2.1) and the obtained with the harvesters significant differences can be seen in the order of magnitude of the output power. This is why the best option is use the geometry (G1) that provides better results and then find the inferior limits where the harvesters can be included. Next results show how adding a tip mass to the harvester can improve its performance. The simulations at this stage where made with the same conditions provided by the lifting surface of table 5.1 for the geometry G1 and the piezoelectric layers of PZT 5J. Table 5.5 shows the input data.

Initial G1 parameters

a	L	W	t_s	t_p	t_{total}	ρ_s	ρ_p	ρ_{eff}	m
0,77	112,5	10	0,14	0,27	0,68	2700	7700	6670	-
m/s^2	mm	mm	mm	mm	mm	kg/m^3	kg/m^3	kg/m^3	g

Table 5.5 Parameters set for harvester G1 tests

Length L and mass m change depending on the addition of the tip mass dimensions L_0 , m_0 . The total length of the beam will not increase since it is forced to be $L_0 + L = 112.5 mm$. The width will not be changed as well to preserve the aspect ratio. Table 5.6 show the values obtained for 10 different tip mass dimensions.

L	112,5	111,5	110,5	109,5	108,5	107,5	106,5	105,5	104,5	103,5	102,5	mm
W	10	10	10	10	10	10	10	10	10	10	10	mm
L_0	0	1	2	3	4	5	6	7	8	9	10	mm
m	5,1	5,21	5,33	5,44	5,56	5,67	5,79	5,9	6,02	6,13	6,25	g
f	22,81	22,77	22,73	22,69	22,65	22,61	22,57	22,54	22,5	22,47	22,44	Hz
P_{out}	83,74	90,15	96,68	103,33	110,08	116,93	123,86	130,09	137,91	145,01	152,13	μW
V_p	3,80	3,52	3,68	3,83	3,97	4,11	4,24	4,40	4,52	4,67	4,83	V
Z	5,40E-4	5,58E-04	5,76E-04	5,94E-04	6,11E-04	6,29E-04	6,45E-04	6,61E-04	6,67E-04	6,92E-04	7,07E-04	mm
P_ρ	4,9561	5,2083	5,4473	5,689	5,93	6,174	6,4185	6,663	6,908	7,15	7,399	mW/kg
R_l	135,89	138,11	140,22	141,97	143,36	144,37	144,99	148,39	148,26	150,98	153,4	$k\Omega$

Table 5.6 Geometry and output results with tip mass

For mass tip addition tests, only length is increased instead of adopt other solutions like change the thickness for the reason that MAV thickness (mainly airfoil thickness) is limited and increasing this value in the harvester could lead to be unable to place the device inside the structure.

The output values are presented in figures 5.12 to 5.14 as well, so that the tendency of the results is easier to identify.

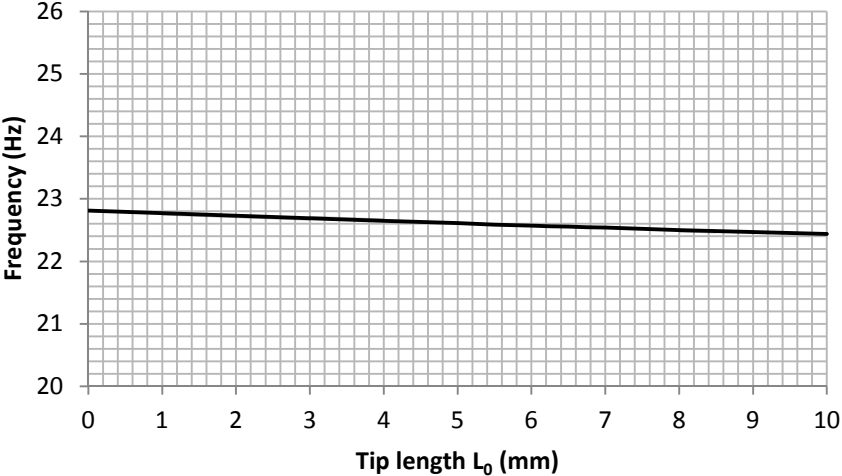


Figure 5.12 Frequency vs. tip length

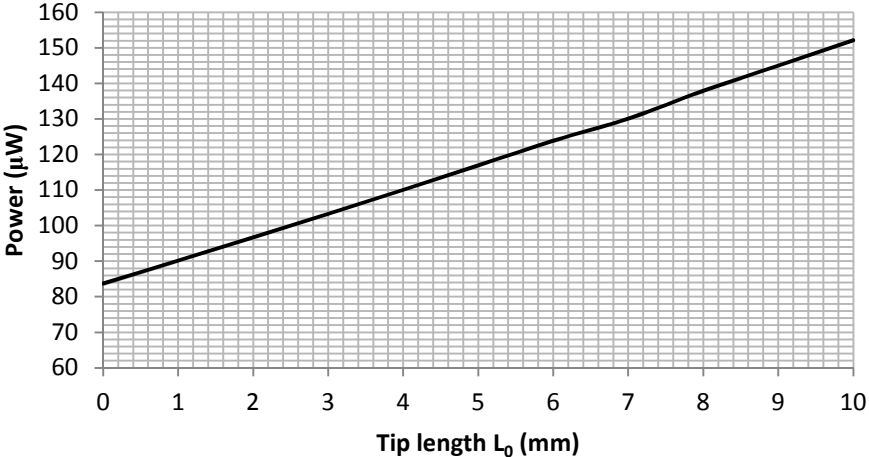


Figure 5.13 Power vs. tip length

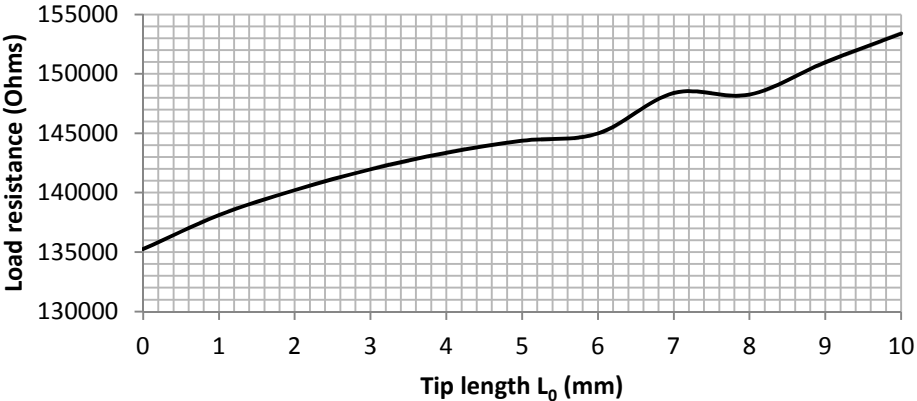


Figure 5.14 Resistive Load vs. tip length

The first important results are the frequency decrease; adding a tip mass does not affect significantly the frequency because the length of the beam remains equal. The CG moves away from the root of the beam but it is insignificant so the effect on the frequency is barely noticed achieving only a reduction of 0,4 Hz.

Figure 5.15 shows another kind of frequency decrease, this time the simulation was run with another dimensions ($L = 55mm$ and $W = 31mm$) but now it is allowed to increase the total length of the beam with the tip mass. As seen in the figure, the frequency decreases faster but the total length of the beam tends to the same as the proposed in the current design. But proceeding this way has still another negative feature; the total mass of the harvester would be higher penalizing on the endurance compared to the power obtained from the vibrations.

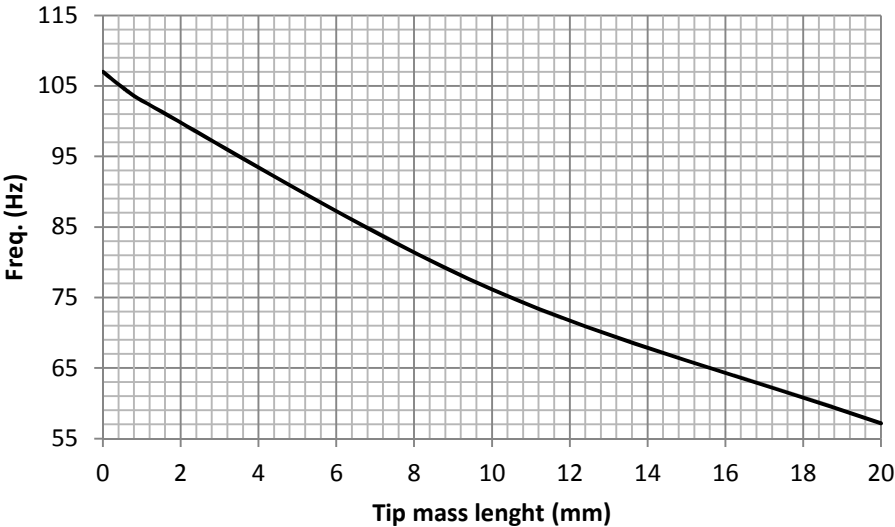


Figure 5.15 Frequency vs. tip mass for a non-fixed total length

The power however, follows a linear progression and reaches higher values with a larger tip mass. In this case the effect of the tip mass is relevant because the bending moment increases with the mass and so does the strain on the surface of the beam, it is not the geometry that affects the power but the dynamics of the beam. In this study, it is only been considered a 10mm long tip mass for reasons that will be explain in the following lines, but if the tip mass increases (and the piezoelectric layer length decrease to maintain the total length) a maximum value that cannot be exceeded will be found due to the lack of piezoelectric material. In any case, the addition of the tip mass is very helpful to increase the power as well as the power density reaching an increase of practically a 100% relative to the power with no tip mass. As it will be seen, the higher values are not really reliable though, because the behavior of the load resistance seems to diverge.

In effect, the load resistance has a positive growing trend that slowly becomes steadier, but suddenly there is a disruption followed by a higher growing behavior. This fact leads to think that the theory used to model the beam is no longer valid and therefore the values obtained for tip masses higher than 5mm long are not trustable. Note that this disruption is only noticed in the resistive load and does not affect the rest of the parameters.

Thus, after the discussion of results on the tip mass effect, the best performance that the bending beam can provide with reliable data is listed in tables 5.7 and 5.8.

Basic beam							Tip mass				Total Dimensions			
ρ_s	ρ_P	ρ_{eff}	L	W	t_s	t_P	ρ_0	L_0	W_0	t_0	L_{total}	W_{total}	t_{total}	m
2700	7700	6670,6	107,5	10	0,14	0,27	7400	5	10	0,68	112,5	10	0,68	5,68
$\frac{kg}{m^3}$	$\frac{kg}{m^3}$	$\frac{kg}{m^3}$	mm	mm	mm	mm	$\frac{kg}{m^3}$	mm	mm	mm	mm	mm	mm	g

Table 5.7 Geometrical parameters of the proposed harvester

Output parameters		
$V_{p_{max}}$	f	$P_{density}$
4,1	22,61	6,174
V	Hz	mW/kg

Table 5.8 Output values of the proposed harvester

5.4 Performance results

The cantilevered harvester has already been designed. This section describes how the harvester affects to the performance of a MAV. Remember section 2.1 where the key parameters defining a general MAV were deduced from the existing models, the table summarizing the data is shown again for the comfort of the reader:

	Fix. Wing	GTOW (g)	Cruise Speed (m/s)	Max. L/D	Endurance (min)	Power source	Energy Density (W·h/kg)
main	Yes	125	15	6	20	Battery + harvesters	140 +harv. Energy Density
Min.	-	100	14	5.5	15	-	-
Max.	-	180	20	7	25	-	-

The analysis of the endurance is made with the formulation described in section 3.2: the normalized endurance, which is expressed by equation 5.12 and taken from section 3.2 as well.

$$\frac{\Delta t_E}{t_E} \approx \frac{\Delta m_B}{m_B} - \frac{3 \Delta m_B + \Delta m_{ST} + \Delta m_{harv}}{2 m_T} + \frac{p_{harv} \Delta m_{Harv}}{p_{ave} m_B} \quad (5.12)$$

As the reader may notice in the above formula, the mass of the MAV is distributed in different blocks based in the subsystems comprising the vehicle. The breakdown of the mass has been chosen analyzing the information provided in [1]. The percentages of each mass block may change depending on every MAV but in general the ratio between every mass block and the total mass differs poorly between different MAV models. Table 5.9 shows the distribution used to perform the tests in this project.

Model	Structure	Payload	Propulsion	Electronics
Black Widow	17%	12%	62%	9%
MICOR	18%	9%	70%	9%
Microbat	24%	0	58%	18%
Selected	16%	10%	65%	9%

Table 5.9 Vehicle mass fractions for three MAV and the fractions adjusted for the study

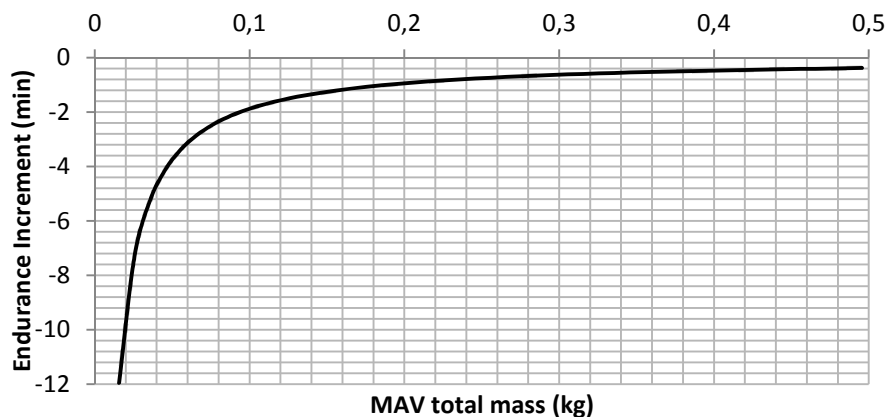


Figure 5.16 Endurance improvement vs. mass of the MAV, using normalized endurance expression

Figure 5.16 shows a clear result. Adding the piezoelectric harvester only leads to losing minutes of flight. If the mass of the MAV is increased (keeping the mass of the harvester), then the flight endurance is not so impaired. The maximum loss would be 22,2 seconds but it would be impossible to get a positive result. The reason of the endurance loss is caused by the small specific power (W/kg) that the harvester is able to provide. The accelerations acting on the root of the beam are very weak making impossible to force the beam getting stronger stress values; therefore the specific power does not increase enough. But the specific power is not the only problem, another important feature is the mass added by the harvester. In the case showed in figure 5.16, the harvester is added as an extra mass to the MAV, structure, payload, electronics and propulsion remains intact, so equation (5.12) is reduced to the following expression, and is then used to perform the graphic of figure 5.16.

$$\frac{\Delta t_E}{t_E} \approx -\frac{3}{2} \frac{\Delta m_{harv}}{m_T} + \frac{p_{harv} \Delta m_{Harv}}{p_{ave} m_B} \quad (5.13)$$

$$\Delta m_B = \Delta m_{ST} = \Delta m_P = 0 \quad (5.14)$$

The contribution of the first term on the right side of equation (5.13) is very high compared to the positive term involving the specific power. So an alternative solution must be designed in order to reduce or ban the effect of the term:

$$-\frac{3}{2} \frac{\Delta m_{harv}}{m_T} \quad (5.15)$$

Or in the general form:

$$-\frac{3}{2} \frac{\Delta m_B + \Delta m_{ST} + \Delta m_{harv}}{m_T} \quad (5.16)$$

In effect, there is a solution that can cancel the negative term. The idea is to implement the harvester with a double function, be the actual harvester and be part of the structure of the MAV as well. This can be pictured as a fixed wing but instead of being completely made of foam, or composite material the piezoelectric harvester would be a structural beam in the skeleton of the MAV substituting part of the original material.

If this was the case, then $\Delta m_{harv} = -\Delta m_{ST}$. Since the batteries will not change their mass $\Delta m_B = 0$. Leading to:

$$-\frac{3 \Delta m_B + \Delta m_{ST} + \Delta m_{harv}}{2 m_T} = 0 \quad (5.17)$$

The endurance now is expressed by the following equation:

$$\frac{\Delta t_E}{t_E} \approx \frac{p_{harv} \Delta m_{Harv}}{p_{ave} m_B} \quad (5.18)$$

This expression can only be positive and ensures an increase of the flight time. Taking into account that the effect of this term is considerably smaller than the negative term of equation (5.15), the prediction of the results leads to think that the positive contribution may not be significantly high and it has no impact on the endurance of the MAV.

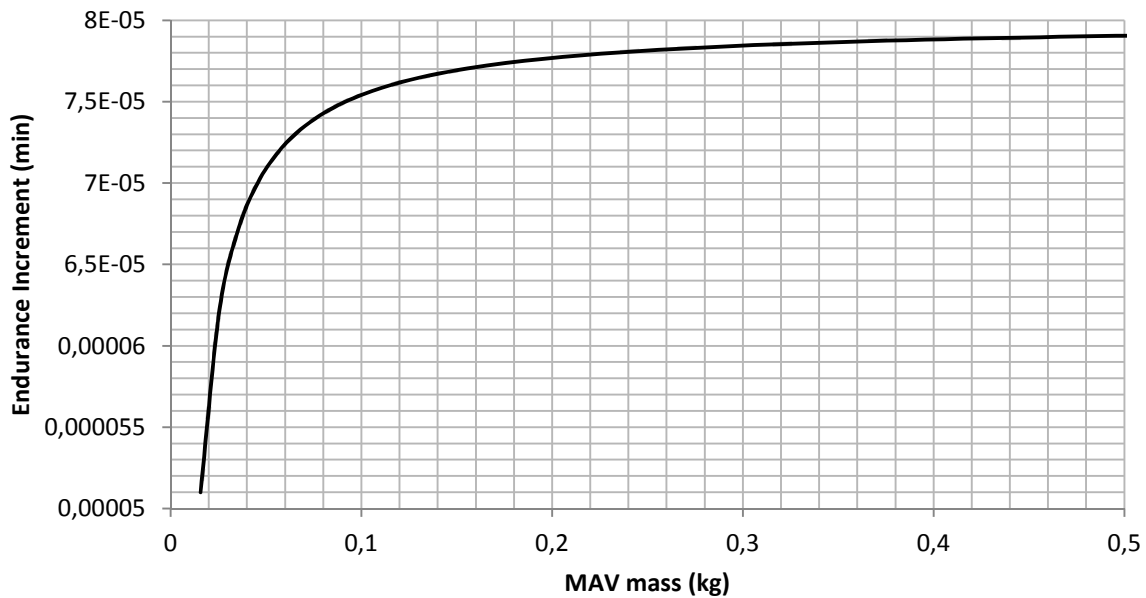


Figure 5.17 Increment of the endurance vs. the total mass of the MAV

After the graphic representation (Figure 5.15), the increment of the endurance is completely unnoticed which to the same conclusion: With the current technology, the specific power is too small to provide extra flight time.

5.5 Evaluation of the solution

The cantilevered harvester seems to be a solution applied to an incorrect range of dimensions. It would be a suitable solution if the external conditions affecting the MAV, specifically the base accelerations, were higher. The maximum specific power that a piezoelectric can provide may be enough to power another kind of vehicle that require less energy, then again, the dimensions of the

harvester would be forced to reduce making difficult to confirm or deny a positive solution in terms of power production.

In terms of frequency excitation, the results are not positive either. The target of 0,8 Hz is too small for the restrictions imposed by the MAV, making possible only a reduction of the frequency until 20 Hz, a frequency only achievable forcing the harvester to be as large as possible. It looks like the piezoelectric technology has a better application for medium and high frequency conditions if the configuration implemented is a cantilever beam.

To sum up, an alternative solution for the implementation of a cantilever harvester in an MAV should suit the two main requirements discussed in the previous paragraphs. It must be subjected to a medium/high frequency excitation environment and must be located in a place where it could take profit of high base accelerations.

If placing the harvester inside the MAV is not a solution, then the first option that comes to mind is place it outside the vehicle as an aerodynamic appendix. The direct contact with the air stream may induce higher stress in the harvester improving the specific power. A resizing would be necessary, not only to optimize the dimensions, but mainly to avoid aerodynamic problems on the surface of the MAV, namely a dramatic increase of the drag that could vanish a possible benefit from the harvester electric power supply.

A complement for any other useful solution for the implementation of this kind of harvesters on MAVs is the design of clusters. Clusters are a connection of various harvesters. If the specific power produced is enough but the output power needs to be higher, the connection in series or parallel of various devices would be the easiest solution instead of designing a larger and more complex harvester. In case of use the clusters as a way to increase the endurance it will end failing due to the mass addition in front of the power supply. That is why the target using cluster would not be increase endurance but to be used as a way to power distributed microelectronics in MAVs.

5.6 Validation

After the deep study of the configuration and due to the rather negative results, the validation of the work done is more than a merely prove of the reliability of this thesis but a way to find out if there were still a possibility to implement this configuration in such a way that permits achieving positive results. The literature is plenty of electromechanical models and cantilever harvester papers (see bibliography) and in this section it will be commented some of them comparing its results with the ones obtained in the project.

Since the code used to develop this study was incomplete, a first validation was made to check whether if the completion of the code was successful or not. To do so, a replica of the simulation done by *du Toit* [12] about a PZT 5A cantilever harvester was made leading to the same values, a fact that confirmed the successful completion of the software. To see the comparison between the values of the original study with the ones of the thesis please refer to annex B, where power, voltage and tip displacement graphs are plotted.

The next part of the validation refers to the results obtained under the restrictions imposed in this project. This would be a base acceleration smaller than 1 m/s^2 with harvesters made of PZT type piezoelectric layers. As it has been already said, the literature is extensive on this topic but there is no information about the implementation on MAVs. That makes difficult to find simulation papers with similar conditions. However, it is possible to check different parameters separately due to the relation of the geometrical dimensions of the beam with the resonance frequency. Thus in *Wang et al* [16] a simulation with a cantilever harvester, whose parameters are reproduced in Table 5.10, is carried out.

Item	Value
Piezoelectric plate, ρ_p (kg/m ³)	7500
Substrate plate density, ρ_s (kg/m ³)	8920
Piezoelectric plate compliance, S_{11}^E (m ² /N)	1.65×10^{-11}
Piezoelectric plate stiffness, C_{11}^E (GPa)	60.6
Substrate plate stiffness, C_1 (GPa)	113
Strain constant, d_{31} (C/N)	-2.74×10^{-10}
Stress constant, e_{31} (C/m ²)	-16.6
Vacuum permittivity, ϵ_0 (F/m)	8.854×10^{-12}
Absolute permittivity, ϵ_{33}^T (F/m)	$3400\epsilon_0$
Absolute permittivity, ϵ_{33}^S (F/m)	$2372\epsilon_0$
Beam length, L (mm)	60
Beam width, b (mm)	20
Thickness of piezoelectric layer, h_p (mm)	0.2
Thickness of substrate layer, h_s (mm)	0.3
Damping ratio of SDOF elastic system, ζ_1	0.002
Damping ratio of piezoelectric beam, ζ_2	0.02

Table 5.10 Parameters for a cantilever harvester simulation in *Wang et al* [16]

The dimensions of this harvester are similar to the ones shown in section 5.3. Table 5.3 and Figure 5.11 show that G4 ($L=64,29 \text{ mm}$, $W=17,5 \text{ mm}$, $t=0,27 \text{ mm}$) and G5 ($L=56,25 \text{ mm}$, $W=20.0 \text{ mm}$, $t=0,27 \text{ mm}$) harvesters' dimensions are similar and the resonance frequency lay in the same range close to 80 Hz.

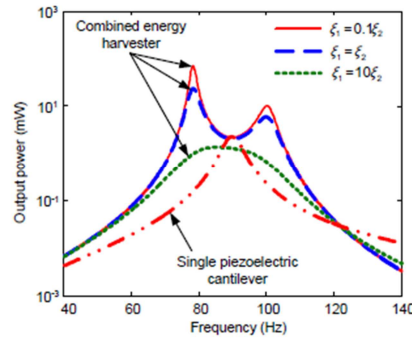


Figure 5.18 Power vs. Frequency from Wang et al [16] study of a cantilever harvester

The frequency has some deviation due to the length of G4 and G5 that are not exactly as the ones in [16]. About the power output what can be seen are higher values, the base excitation driven in this experiment was $1g$. Hence, makes sense that the power is two orders of magnitude higher than the obtained in figure 5.11. The same happens with the load resistance.

The model is contrasted as well with the FE software ANSYS[®] showing relative errors around 1,5 % which proves the validity of the code as a secondary approach.

Two studies by Anton et al [13] [17] use the piezoelectric effect in UAVs with larger dimensions than the ones considered in the project. However, it is a useful analysis to compare the improvement effect on flight endurance. The harvesters tested in his studies are a {3-3} mode spar configuration placed inside the wing without structural functions. There are also two different alternatives depending on the material used, both from composite origin, to reduce the weight as much as possible. The dimensions of both devices are shown in Table 5.11:

Property	Symbol	Macro-Fiber Composite	Piezoelectric Fiber Composite
Device length	l_p	102 mm	145 mm
Device width	w_p	16 mm	15 mm
Device thickness	t_p	0.3 mm	0.3 mm
Device mass	m_p	3.0 g	2.0 g

Table 5.11 Physical properties of the piezoelectric devices considered in Anton et al [13]

Note that the dimensions correlate very well with the ones obtained in the results chapter of this project. Table 5.12 corresponds to the parameters of the cantilevered device:

Total Dimensions			
L_{total}	W_{total}	t_{total}	m
112,5	10	0,68	5,68
mm	mm	mm	g

Table 5.12 Physical properties of the piezoelectric devices designed in this project

The total thickness and the width differ but keep staying in the same order of magnitude, similarly happen to the mass of the device.

The endurance result of *Anton et al* [13] studies lead to similar conclusions to those obtained in the course of this project. Figure 5.22 shows the best case scenario of the simulations done in [13].

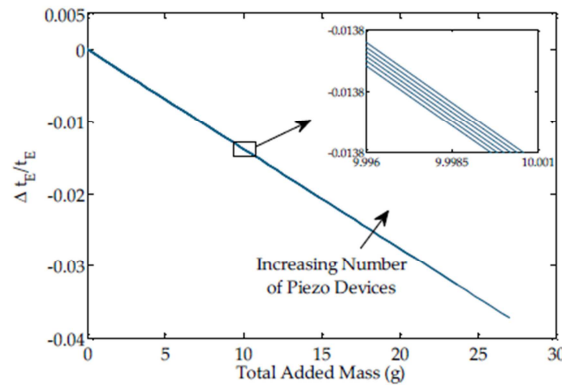


Figure 5.19 Normalized endurance vs. added mass by the harvester

The results of the simulation show that a net loss in flight time occurs for all but the fully multifunctional case where the overall aircraft mass remains unchanged (that is point [0,0] in figure 5.22). A fully multifunctional case refers to a piezoelectric that has extra features like be part of the structure, or even easier, a device that does not affect the overall weight of the MAV compared to the original vehicle.

Basically the conclusion is the same for both *Anton et al* studies [13] [17] and the current project, while the focus of a piezoelectric system is not on achieving an increase in flight time, the goal is to choose a design in which the flight endurance does not suffer.

As a final remark, it is worth to mention the specific power density obtained from the same studies compared to the ones of the thesis. While in [13] for both harvesters the specific power densities are $P_{MFC} = 3,77 \text{ mW/kg}$ and $P_{PFC} = 5,05 \text{ mW/kg}$, while the cantilevered design provides $P_{cantilever} = 6,18 \text{ mW/kg}$, proving not only the validity of the results but the choice of use mode {3-1} as a main piezoelectric distribution. Remember that the discussion about the mode used for the cantilevered harvester showed that the lack of alignment of the electric field between the electrodes tend to worsen the fact that the piezoelectric effect is stronger in {3-3} mode making {3-1} mode achieve higher power values.

6 Theoretical approach on an external device configuration.

In view of the results shown in the previous section, it seems necessary another point of view of the problem, which is finding a different placement for the piezo-harvester. The goal is to increment the acceleration applied on the harvester's body, however this means placing the device outside the MAV so the flow can interact along with the base acceleration (produced by the MAV structure), hence providing an extra force of aerodynamic origin.

This approach raised some difficulties that have led this project to avoid any simulated or experimental study. That is why this chapter aims to show the reasons of the taken decision based on the results that have been already exposed in the previous chapter as well as studies of external bibliographic sources and the limitations for implementing a code based on the inner device approach.

6.1 Initial planned solution

The first solution considered to analyze the external device was to improve the code used in section 5, adding the aerodynamic force to the base excitation and hence obtain results of the combined accelerations. In order to carry on with the aerodynamic excitation, the main point was to use results of previous studies on MAVs to perform the tests; in particular the thesis by *Camara* [15] was the first option because of the study of the vortical flow in sinusoidal leading edge wings. The same source was used to evaluate the base acceleration in the previous chapters, so at first glance it is a good choice.

The main problem that faced this solution was the linkage between the code already built and the output of the flow studies, specifically how to add an extra excitation over the device that acts as a base acceleration. Let us not forget that the code used in the thesis is based in a cantilever beam configuration, thus the addition of extra excitation must be consequent with the boundary conditions of the problem. That is really a big issue because a cantilevered beam subjected to a free stream activates not only the bending modes but also the torsional modes, changing in great measure the physics of the problem. Aside of the mechanical behavior, there is the coupling effect with the piezoelectric material and then adding a time depending turbulent flow would complicate in highly the study of the external device approach.

As a result, all these complications lead to build a specific code only for the study of this particular case. It is not an impossible task; however the time and effort needed to create a reliable code are out of the range for this thesis, although it would be possible if there is a continuation (in future studies) focused in this approach of the MAVs piezoelectric harvesters.

Needless to say that before to proceed with such a work, the feasibility of the solution should be carried out in order to prevent undesired or unusable results. The last section of this chapter is dedicated to this topic and although there are not really high expectations of the feasibility of outer piezoelectric devices there is not a solid answer denying the study of this issue. The discussion will be explained after showing some other studies related to immersing a piezoelectric harvester in an air flow.

6.2 Other studies

After the difficulties faced in the proposed solution to approach the outer device configuration, the use of published studies in the literature was an incentive to continue investigating how to solve the problem. Here are included the considered works, their approach and the problems that were faced when considering its application.

6.2.1 Double-Lattice method for aero-elastic vibrations modeling

The idea is developed by *De Marqui and Vieira* [18] and the main point of the paper is to combine the doublet-Lattice method with the electro-mechanical coupled equations (already developed in section 4.2) to obtain the output power produced by both base and aerodynamic excitations. The addition of the aero-elastic behavior is made by a linearized formulation for the oscillatory, inviscid, subsonic lifting surface theory which relates the normal velocity over a surface with the aerodynamic loads caused by the pressure distribution.

The formulation is derived from flow equation for unsteady potential flow. The potential of a doublet is the solution used to solve the Euler equations and hence obtain the unsteady aero-elastic behavior as well as the resultant differential pressure across the surface of a wing or a lifting surface in this case

The discretization of the thin lifting surface includes a doublet in each element. Then, solving the equation for each element leads to obtain a matrix of influence Q that will be added to the electro-mechanical model.

This approach was a good solution for the study of the outer device configuration. Nevertheless, the problems mentioned at the beginning of the chapter still remain. Those are the addition of torsion modes besides the bending ones and the necessity of build a new code to work with. This paper was used as a validation of the primary idea exposed in the section before but it was an aware (too), of the complications facing the development of the study which ended up with the decision of avoid any study because of possible unreliable results, which in turn could affect negatively on the project.

6.2.2 T-shaped cantilevers subjected to an air stream

The paper described by *Kwon* [19] is an experimental description of a T-Shaped structure subjected to an air stream. The idea is to reach the flutter frequencies of the beam to obtain a sustained and slightly constant power output. The following figure is a scheme of the layout:

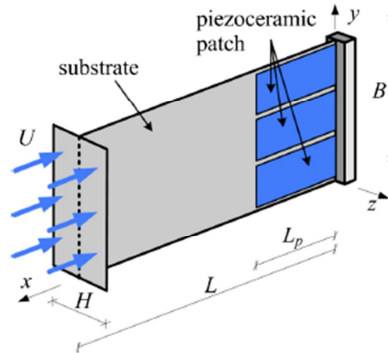


Figure 6.1 Layout of the T-shaped cantilever beam from *Kwon* [19]

The beam is then introduced in the wind tunnel where the wind velocity can be adjusted, the piezoelectric electrodes are connected to a multimeter and the displacement is captured by a CCD camera and using image processing techniques.

Although the layout is considerably different from the one proposed originally in this thesis, the advantage is that it could have been used for validation of possible studies. There are empirical correlations that complete the experimental data which may be used for our cause.

Again, the possibility to investigate through this line was questioned because of the dimensions of the piezoelectric layers, and the whole device in general. The external appendices that an MAV can afford to add outside of the fuselage must be very small in order to avoid drag problem, loss of lift or even loss of endurance by weight addition. Thus, the possibility of using the empirical correlation for smaller devices and also that do not match with the geometry of the proposed paper is highly questionable.

6.3 Feasibility of the configuration

In view of the previous issues to carry on with the study of an external device on MAVs, a natural question came out, motivated largely by the results obtained in the study of the embedded piezoelectric approach. That is, to question the feasibility of using piezoelectric in MAVs regardless of the position inside or outside the structure of the vehicle. It is clear, that an internal device is not intended to be used as a complementary source of propulsion and even try to use it as a power source for installing extra electronics might be worthless because of the endurance loss. However, for external devices, it happens to be unclear whether if increase the capabilities of the MAV (in

terms of information that is able to gather) is a plausible solution or not. The results of the sources described above indicate that similarly to the internal approach the devices are unable to provide more than 1 mW . The results shown in *Kwon* [19] for a three piezoelectric layers device with dimensions¹³ $L = 100\text{ mm}$, $B = 60\text{ mm}$, $H = 30\text{ mm}$ subjected to a wind speed of $4,6\text{ m/s}$ and a tip mass of $15,5g$ are presented in figures 6.2 and 6.3.

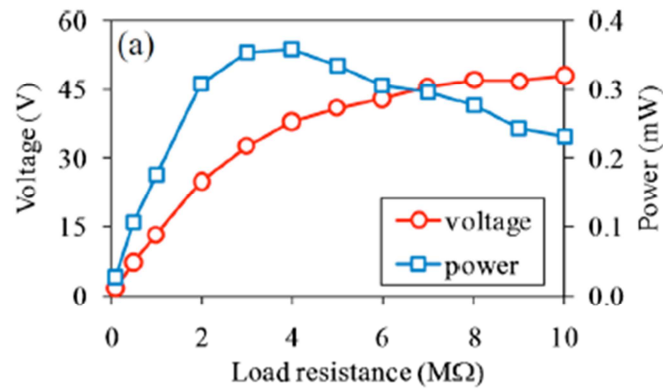


Figure 6.2 Output performance for a T-shape device with 6Hz vibrations from *Kwon* [19]

The power increases until 4 mW if the speed is raised up until 15 m/s which is the target speed of the MAV's point of design of this thesis (see figure 6.3). This is a slightly better result than the one obtained for the internal device. Still the geometry proposed in this paper presents impediments to apply something similar to the fuselage of an MAV. Starting from the mass proof, the weight is much higher than the affordable both for the endurance and the aerodynamics. The size of the complete device is also out of the boundaries and the outputs certainly will not be enough for an increment of the flight time.

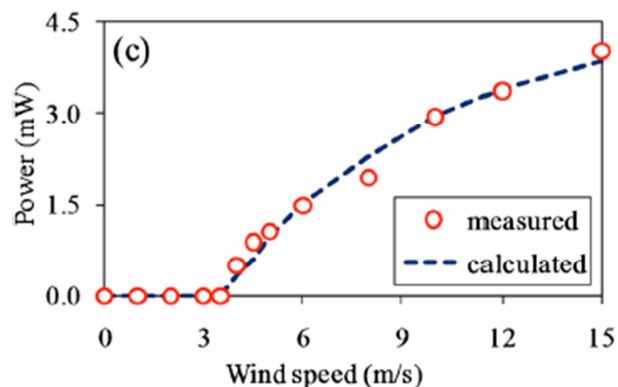


Figure 6.3 Power vs. wind speed comparison from *Kwong* [19]

¹³ The dimensions are in accordance to the nomenclature shown in figure 6.1

Nonetheless, the doubt of the usefulness remains if these devices can be installed in larger MAVs, or safer say small UAVs, where the mass of the harvester is negligible in front of the mass of the vehicle, making it a better solution for the installation of extra features in the MAV.

Then external devices, at first glance, seem better sources of power than the internal device configuration, but the lack of information regarding the vibrations of aero-elastic effects makes it difficult to dismiss or approve this option. Take into account that the conditions where these devices have been tested are different than the ones occurring around a MAV/UAV fuselage. After all the discussion, the most reasonable plan should be a proper study of the flow around an MAV model capturing the acceleration in critical points of the structure and then discern whether it is worthwhile to continue an investigation on this line.

7 Conclusions and future work

The studies performed during this thesis were focused on the assessment of electric power that a cantilever harvester can provide placing the device inside a fixed-wing MAV structure. The objective was using this energy as a primary recharging method to extend the endurance of such vehicles

The results show piezoelectric materials cannot be a primary source for recharging the batteries of the propulsion system. The study of the excitations acting over the structure of an MAV (represented as a sinusoidal leading edge flying wing) revealed low accelerations acting at proximately 1Hz frequencies. Those restrictions were considered when designing the cantilevered harvester leading to power outputs of a few mW at ~ 20 Hz frequencies. Both tasks (reaching the goal excitation frequency and provide enough power to feed the batteries) were infructuous due to size limitation of the harvester and lack of higher excitations. The link between the geometrical shape of the beam and the natural frequency showed the major necessity of high aspect ratio dimensions but the size of the MAV reduce the length and width to a maximum amount that cannot be exceeded. Thus the area of the harvester is limited (as well as the piezoelectric material) and, with the already mentioned excitations, it is not possible to reach the desired output requirements.

An external harvester configuration was also considered but research on literature showed similar results for devices placed in free streams with similar velocities to MAVs. This fact and the complexity to build a code to simulate the behavior of a beam subjected to the air flow discouraged a deeper study of this approach.

The validation of the code used for the simulations along with comparison of cantilever harvester studies ensures the solid results of the thesis. Even in larger scale vehicles, like small UAVs, studies show piezoelectricity is suitable only as secondary power sources, such as feeding electronics of the aerial vehicle. In order to not lose endurance, the devices must have a multifunctional purpose, so that the overall weigh is not increased.

At this point the reader may find discouraging future studies on piezoelectricity as an application for MAVs but certainly what this thesis has reached is to point the strong relation between the behavior of the surrounding environment over the MAV with the harvester performance, which helps to find new situations where this technology has better chances to fulfill positive results.

As an example, think about carrying a larger payload without penalties on the endurance. This branch is currently under study not only for MAVs but for other vehicles and systems with multipurpose tasks.

Another possibility is to study the availability of using the piezoelectric effect in the propulsion system of flapping wing MAVs. This vehicle configuration needs a large amount of continuous power but the batteries cannot typically afford more than 2 minutes of flight time. Taking advantage from the flapping wings as a source of excitation for piezoelectric layers may extend the endurance.

And lastly, the reverse piezoelectric effect is also a challenge. Using a voltage input to make piezoelectric wings flap would reduce the necessity of mechanical parts in the vehicle, reducing weight that can be used for extra features.

Bibliography

- [1] F. Bohorquez y D. J. Pines, Challenges Facing Future Micro-Air-Vehicle Development, vol. 43, *Journal of Aircraft*, April 2006.
- [2] A. Epstein, S. Senturia, O. Al-Midani, G. Anathasuresh, A. Ayon, K. Breuer, K.-S. Chen, F. Ehrich, E. Esteve, L. Frechette, G. Gauba, R. Ghodssi, C. Groshenry, S. Jacobson, J. Kerrebrock, J. Lang, C.-C. Lin, A. London, J. Lopata, A. Mehra, J. Mur, S. Nagle, D. Or, E. Piekos, M. Schmidt, G. Shirley, S. Spearing, C. Tan, Y.-S. Tzeng y I. Waitz, «Micro-Heat Engines, Gas Turbines, and Rocket Engines, The MIT Micro-engine Project,» Massachusetts Institute of Technology, Cambridge, 1997.
- [3] W. J. Wu y B. S. Lee, Piezoelectric MEMS Power Generators for Vibration Energy Harvesting, Taipei: Department of Engineering Science and Ocean Engineering, pp. 135-157.
- [4] D. Guyomar, A. Badel, E. Lefeuvre y C. Richard, Toward energy harvesting using active materials and conversion improvement by nonlinear processing, vol. 52, *IEEE Transactions on*, 2005, pp. 584-595.
- [5] E.Lefeuvre, A.Badel, L. L. A. Benayad, C.Richard y D.Guyomar, A Comparison Between several Approaches of Piezoelectric Harvesting, vol. 128, *Journal De Physique IV*, 2005, pp. 177-186.
- [6] A.Badel, D. Guyomar, E.Lefeuvre y C.Richard, Efficiency enhancement of a piezoelectric energy harvesting device in pulsed operation by synchronous charge inversion, vol. 16, *Journal of intelligent material systems and structures*, 2005, pp. 889-901.
- [7] Y. Jeon, R. Sood, J.H.Jeong y S. Kim, MEMS power generator with transverse mode thin film PZT, *Sensors and Actuators -A: Physical*, n16, pp. 2253-2264, 2005.
- [8] «Piezo Technologies,» 2014. [On line]. Available: <http://www.piezotechnologies.com/Ceramics/Datasheets.aspx>. [Last acces: 16 July 2014].
- [9] PI Ceramic GmbH, PI Ceramic, 2014. [On line]. Available: <http://piceramic.com/products/piezoelectric-materials.html>. [Last acces: 16 July 2014].
- [10] SG3 Knowledge Network OG , PiezoMat, 2014. [On line]. Available: <http://piezomat.org/>. [Last acces: 2014 July 17].
- [11] Arkema Group, Piezotech, 2014. [On line]. Available: <http://www.piezotech.fr/image/documents/22-31-32-33-piezotech-piezoelectric-films-leaflet.pdf>. [Last acces: 20 July 2014].
- [12] M. Du Toit, Modeling and design of a MEMS Piezoelectric Vibration Energy Harvester, MIT, 2005.
- [13] S. R. Anton, Multifunctional Piezoelectric Energy Harvesting Concepts, Blacksburg, 2011.

- [14] J. Wang, Y.-K. Yong y T. Imai, Finite Element Analysis of the Piezoelectric Vibration of Quartz Plate Resonators with Higher-order Plate Theory, Orlando, FL: IEEE International Frequency Control Symposium, 1997, p. 9.
- [15] J. F. D. d. Camara, Controlo Passivo da Perda em Micro-Veículos Aéreos Usando Bordos de Ataque Sinusoidais, Master thesis in Aerospace Engineering, Universidade de Lisboa, 2012.
- [16] h.-y. Wang, X.-b. Shan y T. Xie, An energy harvester combining a piezoelectric cantilever and a single degree of freedom elastic system, *Journal of Zhejiang University-Science A (Appl Phys & Eng)*, vol. 13, n 7, pp. 526-537, 2012.
- [17] S. R. Anton, A. Erturk y D. Inman, An Investigation on Piezoelectric Composite Spars for Energy Harvesting in Unmanned Aerial Vehicles, Blacksburg, VA.
- [18] C. D. M. Jr. y W. G.R.Vieira, Modeling and Analysis of Piezoelectric Energy Harvesting From Aeroelastic Vibrations Using the Doublet-Lattice Method, *Journal of Vibration and Acoustics*, vol. 133, pp. 1-9, February 2011.
- [19] S.-D. Kwon, A T-Shaped piezoelectric cantilever for fluid energy harvesting, *Applied Physics Letters*, nº 97, p. 3, 2010.
- [20] N. Hagood, W.Chung y V. Flotow, Modelling of piezoelectric actuator dynamics for active structural control, *Journal of intelligent Material Systems and Structures: Vol.1*, n 3, pp. 327 - 354, 1990.
- [21] J. P. Thomas, M. A. Qidwai y J. Kellogg, Energy scavenging for small-scale unmaned systems, *Journal of Power Sources*, vol. II, n 159, p. 1494–1509, 2006.

A. ANNEX : Electrical connection for cantilevered harvester

Cantilevered harvesters can be designed with different layouts as it is been shown (section 2.3) when discussing the modes that the harvester could adopt depending on the orientation of the piezoelectric layers. The orientation of these layers with themselves and the direction between the electric field and strain vectors affect the outputs and performance of the harvester. Since mode {3-1} is the only disposition used for testing the harvesters, it is unnecessary to add to the current thesis an annex on how mode {3-3} works. However, there are other configurations involving mode {3-1} where it is important to include extra information to have a full understanding of how the electro-mechanical mode has been applied. Indeed, the modeled harvesters can be designed with multiple piezoelectric elements which mean multiple pairs of electrodes. The electrodes connection change the constitutional equations that have been adapted to compute the behavior of a cantilevered harvester, this annex explains those different connections as well as the changes produced on the constitutional equations.

When in previous sections the use of a three layered beam was selected as the definitive harvester configuration, the mentioned materials forming the beam were only two layers of piezoelectric material and a structural layer between them. This was, a simplification intended to make the reader understand in an easy way the mechanics of the harvester, but as one may expect other layers are necessary to add the connections and isolate the electrodes to avoid undesired short-circuits. The following scheme shows the layers involving two beam configurations:

Uni-morph configuration

Contains 4 layers as shown in figure A.1:

- 2 Electrode layers (black)
- 1 Piezoelectric layer (grey)
- 1 Structural layer (white)

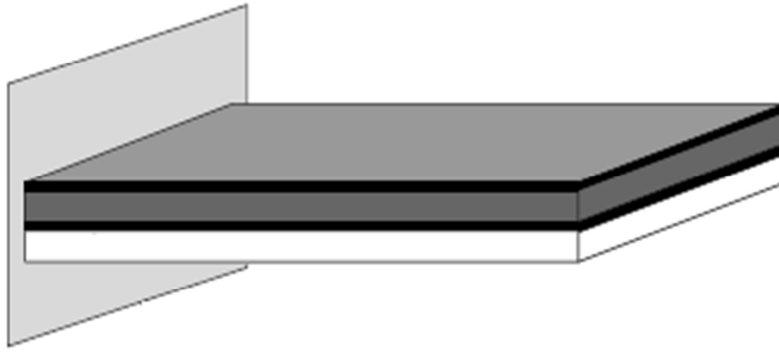


Figure A.1 Layer disposition of uni-morph cantilevered harvester

Bi-morph configuration

A symmetrical approach of the uni-morph cantilevered harvester. It contains an extra pair of electrodes and an extra layer of piezoelectric material, as shown in figure A.2:

- 4 electrode Layers (Black)
- 2 Piezoelectric layers (Grey)
- 1 Structural layer (white)

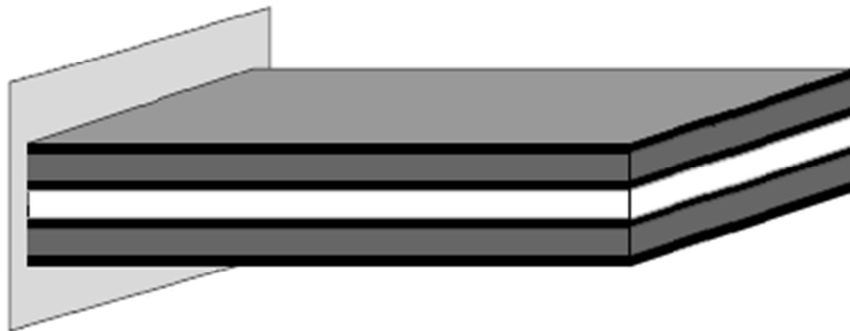


Figure A.2 Layer disposition of the bi-morph cantilevered harvester

A pair of electrodes plus a piezoelectric layer is called an element. These harvesters may include more than two elements if needed, depending on the requirements of the problem. For multiple element harvesters the connection between elements can be in series or parallel and depending on the chosen connection the electro-mechanical model will change in accordance.

Remember from section 4.2 that the coupled piezo-mechanical effect is expressed as:

$$M\ddot{r} + C\dot{r} + Kr + \Theta v = B_f \ddot{w}_B \quad (\text{A.1})$$

$$\Theta^t r + C_p v = -q \quad (\text{A.2})$$

For a single mode study, the equations above are scalar. Remember how in the previous sections was commented the fact that the application of the electro-mechanical model will be applied only using the first model of the beam, thus if the number of elements is one, this statement is true. However, if there are more elements then the equations acquire matrix form. For the bi-morph harvester the equations (A.1) and (A.2) are developed as follows:

$$M\ddot{r} + C\dot{r} + Kr - \begin{bmatrix} \theta_1 & 0 \\ 0 & \theta_2 \end{bmatrix} \begin{Bmatrix} v_1 \\ v_2 \end{Bmatrix} = -B_f \ddot{w}_B \quad (\text{A.3})$$

$$\begin{Bmatrix} \theta_1 \\ \theta_2 \end{Bmatrix} r + \begin{bmatrix} C_{p1} & 0 \\ 0 & C_{p2} \end{bmatrix} \begin{Bmatrix} v_1 \\ v_2 \end{Bmatrix} = -\begin{Bmatrix} q_1 \\ q_2 \end{Bmatrix} \quad (\text{A.4})$$

The subscripts 1 and 2 make reference to the number of elements connected. In order to be able to carry out power optimizations, it is vital to write the previous equations in a scalar form. This is done by considering an equivalent element for the whole harvester. If both equations are added the result reads:

$$M\ddot{r} + C\dot{r} + Kr - (\theta_1 v_1 + \theta_2 v_2) = -B_f \ddot{w}_B \quad (\text{A.5})$$

$$(\theta_1 + \theta_2) r + (C_{p1} v_1 + C_{p2} v_2) = -(q_1 + q_2) \quad (\text{A.6})$$

The single element should be expressed with effective coefficients as indicated in the following equations

$$M\ddot{r} + C\dot{r} + Kr - \theta_e v = -B_f \ddot{w}_B \quad (\text{A.7})$$

$$\theta_e r + C_{p_e} v = -q \quad (\text{A.8})$$

Where:

$$\theta_e v = \theta_1 v_1 + \theta_2 v_2 \quad (\text{A.9})$$

$$\theta_e = \theta_1 + \theta_2 \quad (\text{A.10})$$

$$C_{p_e} v = C_{p1} v_1 + C_{p2} v_2 \quad (\text{A.11})$$

Notice that for a single element harvester the equivalent scalar equation is reduced to the original equations. Nevertheless, the charge q can be expressed in terms of the voltage using the relations with intensity for single or multiple element harvesters:

$$i = \frac{dq}{dt} ; \quad i = \frac{v}{R_l} \quad (\text{A.12})$$

$$\theta_e \dot{r} + C_{P_e} \dot{v} + \frac{1}{R_l} v = 0 \quad (\text{A.13})$$

The next subsections will show how the equivalent terms are found assuming a symmetrical bi-morph configuration¹⁴

A.1. Series connection

For the series connection, the two elements are poled in opposite directions, such as the strains produced above and below the neutral axis generate electric fields that are in the same direction. Figure A.3 shows the connection of the device (right) and the corresponding scheme on the left.

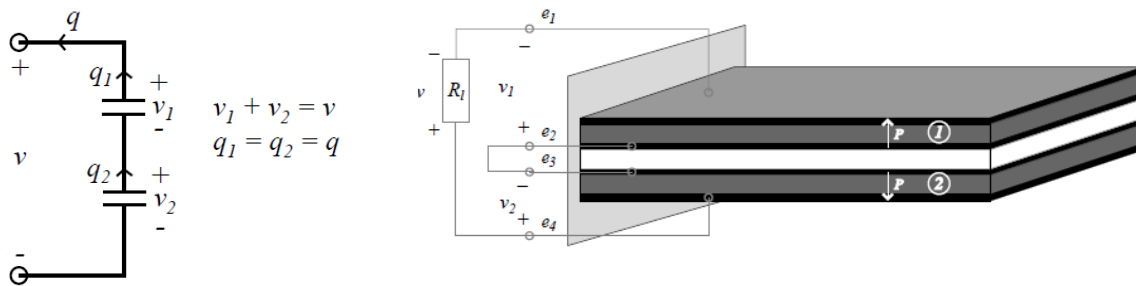


Figure A.3 Series connection for a bi-morph harvester

There are two observations two be noticed:

$$v_1 + v_2 = v \quad (\text{A.14})$$

$$q_1 = q_2 = q \quad (\text{A.15})$$

Now substituting on the governing equations shown at the beginning of the section (expressions (A.5) and (A.6)) leads to:

$$M\ddot{r} + C\dot{r} + Kr - 2\theta_1 v_1 = -B_f \ddot{w}_B \quad (\text{A.16})$$

$$2\theta_1 \dot{r} + 2C_{P_1} v_1 = -2q_1 \quad (\text{A.17})$$

¹⁴ Since Bi-morph configuration contains two elements is enough to show the dynamics of connecting various elements. For more than two elements, the process would be analogous.

Because of the series connection, the charge is unique for the whole circuit $q_1 = q$. Relating q with the intensity and using Ohm's law, the previous equations can be written in terms of the voltage.

$$M\ddot{r} + C\dot{r} + Kr - 2\theta_1 v = -B_f \ddot{w}_B \quad (\text{A.18})$$

$$\theta_1 \dot{r} + \frac{1}{2} C_{p_1} \dot{v} + \frac{1}{Rl} v = 0 \quad (\text{A.19})$$

It is also been used the relations for a symmetrical device, that is: $v_1 = v_2$ and $C_{p_1} = C_{p_2}$ so the effective coefficients for a single device model turn out to be $C_{p_e} = \frac{1}{2} C_{p_1}$, $v = 2v_1$ and $\theta_1 = \theta_e$. Note that the equivalent capacitance is the corresponding term for a two identical capacitors connected in series. Finally, the equations of motion have been reduced to a two scalar expressions and the performance of the system can be analyzed in an easy way rather than having matrix equations.

A.2. Parallel connection

The parallel connection requires that both elements are poled in the same direction so the voltages add when the beam is bent. Figure A.4 shows the connection scheme:

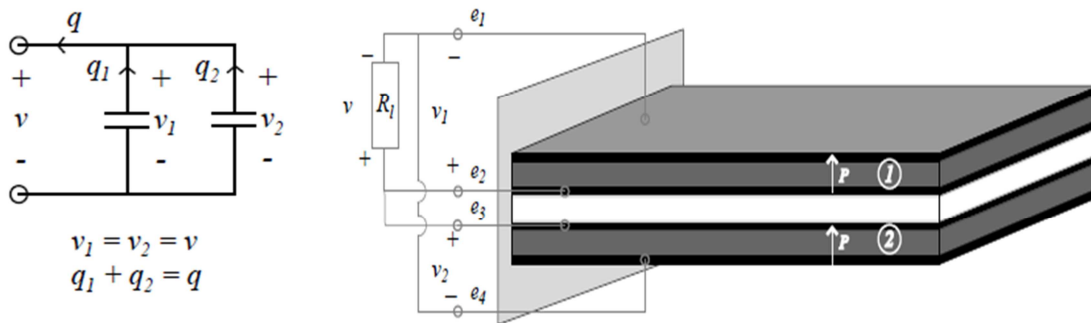


Figure A.4 Parallel connection of a bi-morph harvester

Both elements of the bi-morph configuration are represented as capacitors since their function is produce a voltage between the electrodes. In addition, the parallel connection of capacitors has the properties:

$$v_1 = v_2 = v \quad (\text{A.20})$$

$$q_1 + q_2 = q \quad (\text{A.21})$$

Introducing these two definitions in equations (A.5) and (A.6) both expressions are written in terms of the voltage and charge. But then again, remembering the relations $i = \frac{dq}{dt}$ and $v = iR_l$ the new equations become a function of the voltage as happened with equations (A.7) and (A.13):

$$M\ddot{r} + C\dot{r} + Kr - (\theta_1 + \theta_2)v = -B_f\ddot{w}_B \quad (\text{A.22})$$

$$(\theta_1 + \theta_2)\dot{r} + (C_{p_1} + C_{p_2})\dot{v} + \frac{1}{Rl}v = 0 \quad (\text{A.23})$$

For convenience, the effective coefficients are implemented in the single electrode system model, being: $\theta_e = \theta_1 + \theta_2$ and $C_{p_e} = C_{p_1} + C_{p_2}$.

Note that the results look intuitive since the effective capacitance for two capacitors in parallel simply the sum of individual capacitances. If the bi-morph beam were symmetric ($\theta_1 = \theta_2$ and $C_{p_1} = C_{p_2}$) then the equivalent coefficient are rewrote as follows:

$$\theta_e = 2\theta_1 \quad C_{p_e} = C_{p_1} \quad (\text{A.24})$$

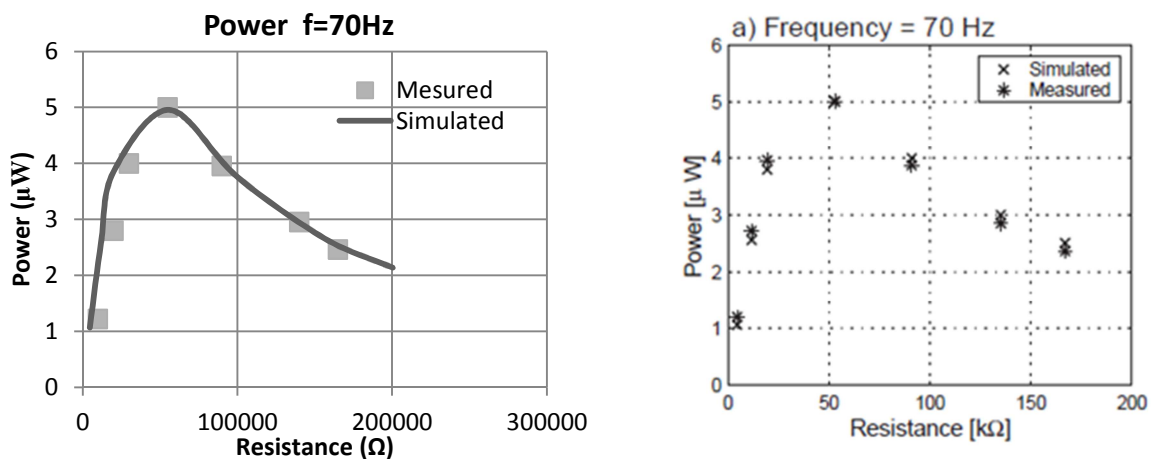
B. ANNEX : Validation of the code

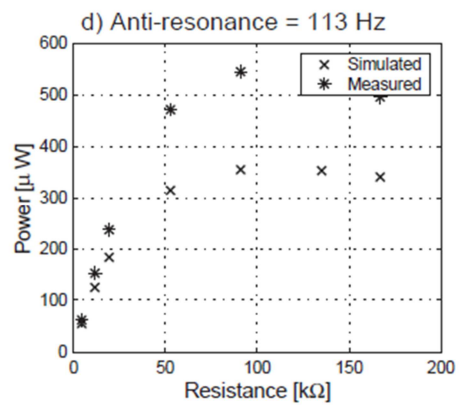
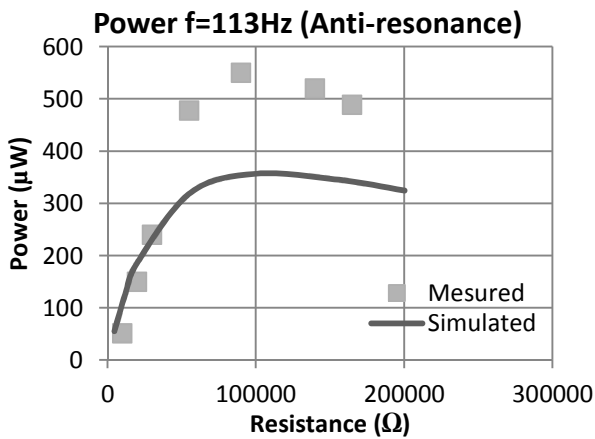
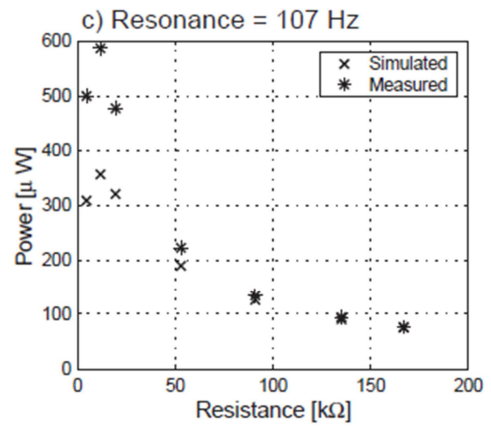
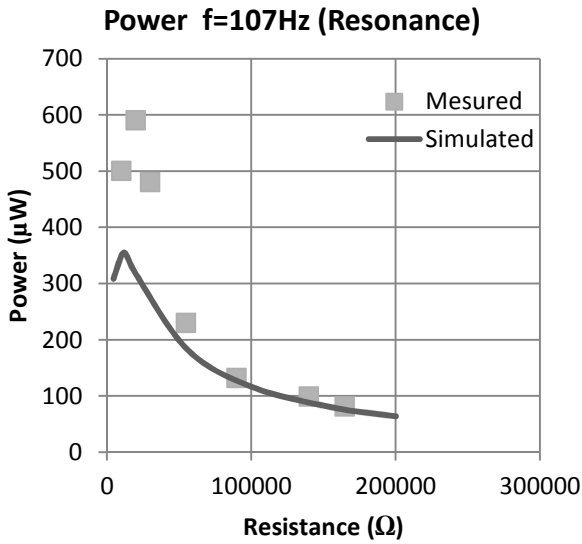
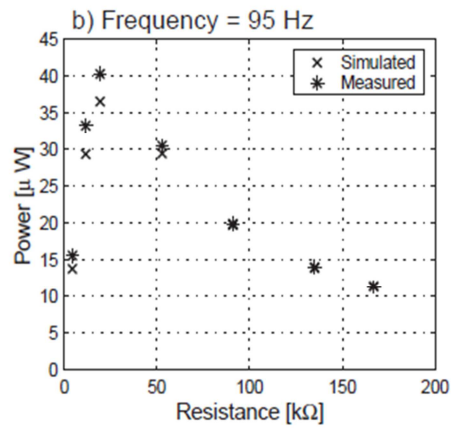
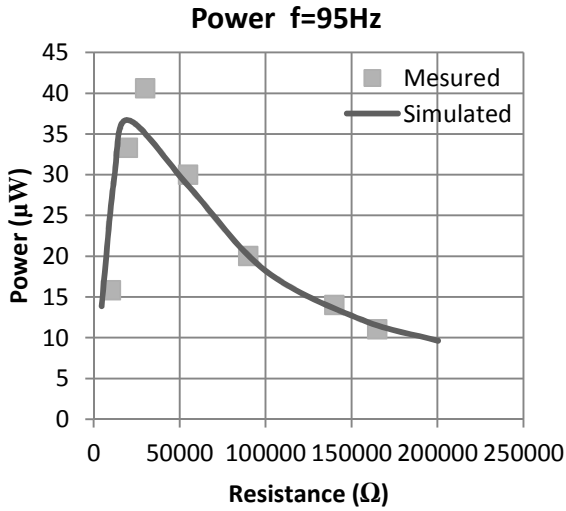
The code used to analyze the design of the cantilever harvester was based on the work of *du Toit* [12] and expanded with some additional features. Nevertheless, it was mandatory to check if both the completion and the improvements made were correct or not. The following figures are the replica of the simulation carried out by *du Toit* [12] with the input parameters listed below:

Material property (beam configuration †)	Used	Published	Ref.
Published properties used			
ρ_p [kg/m^3]	7800	7800	[104]
c_{11}^E * [GPa]	66	66	[104]
d_{31} [m/V]	-190×10^{-12}	-190×10^{-12}	[104]
Measured properties			
Device length, L [mm]	63.5	63.5	[104]
Device width, b [mm]	31.8	31.8	[104]
Piezo layer thickness, t_p [μm] ‡	270	270	[104]
Structure layer thickness, t_s [μm] ‡	140	130	[104]
Device mass [$grams$]	10.564	-	-
Capacitance (constant stress), C_p^I [nF]	52.8	59.1	-
e_{31} * [C/m^2]	-14	-	-
Calculated properties			
ρ_s [kg/m^3]	7165	9000	[100]
ϵ_{33}^d [F/m]	$1800 \times \epsilon_0$	$1800 \times \epsilon_0$	[104]
Elastic stiffness, structural layer, c_s [GPa]	100	105	[100]
ϵ_{33}^s * § [F/m]	$1500 \times \epsilon_0$	-	-

Figure B.1 Table showing the parameters for the device simulation, courtesy of *du Toit* [12].

The results for power, voltage and tip displacement are compared for various frequencies including resonance and anti-resonance in figures B.2, B.3 and B.4. Note that in the replica the experimental results of [12] have also been plotted for a major appreciation on the validity of the simulation.





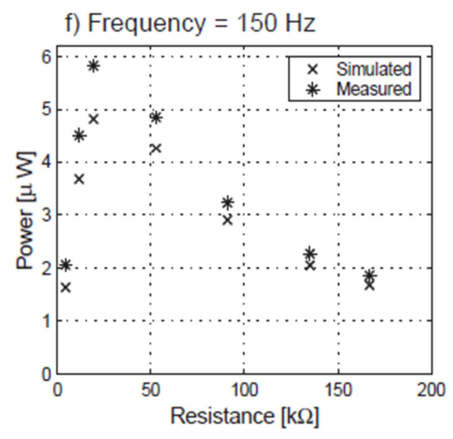
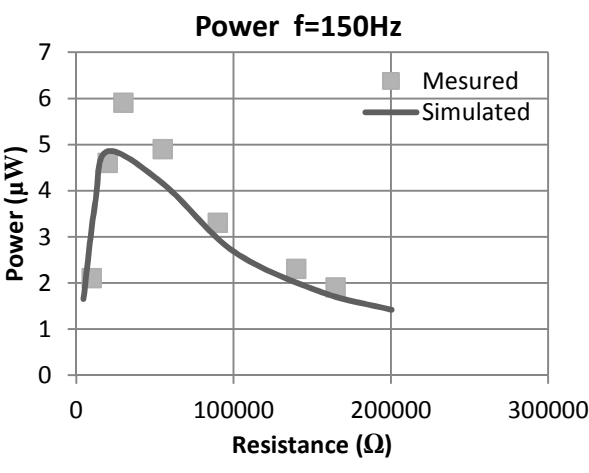
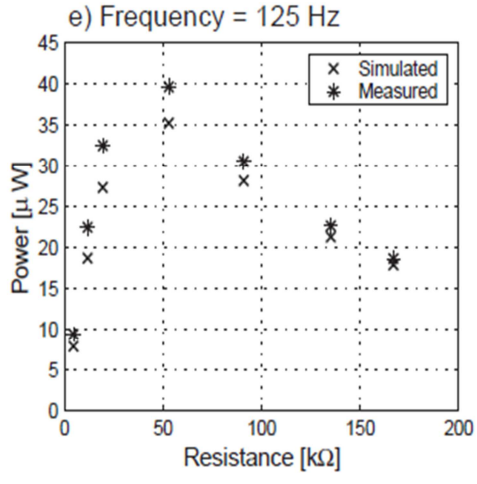
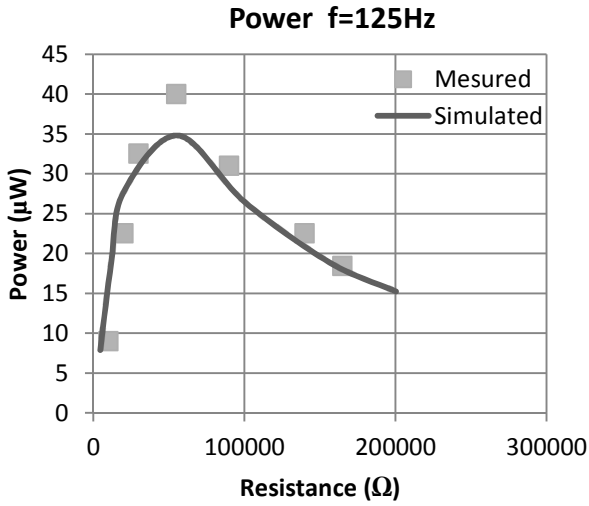
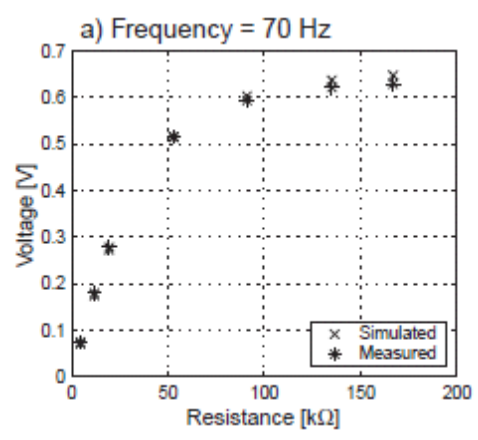
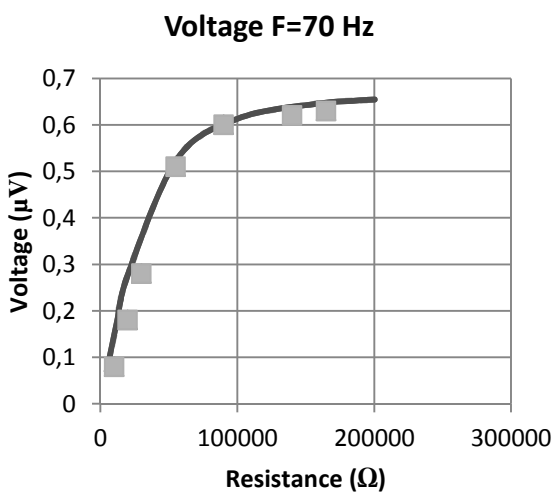
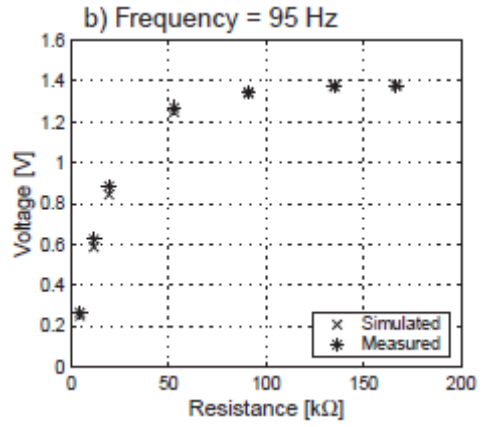
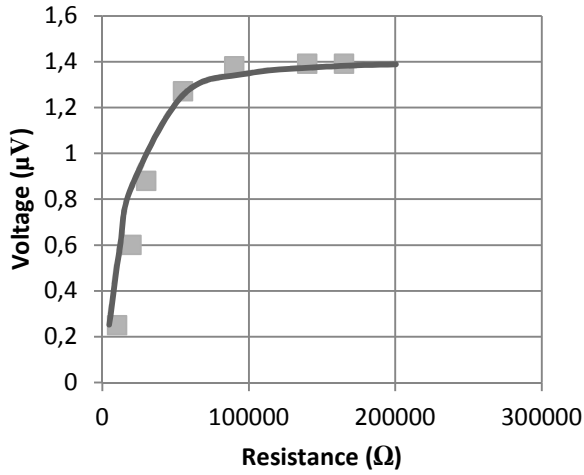


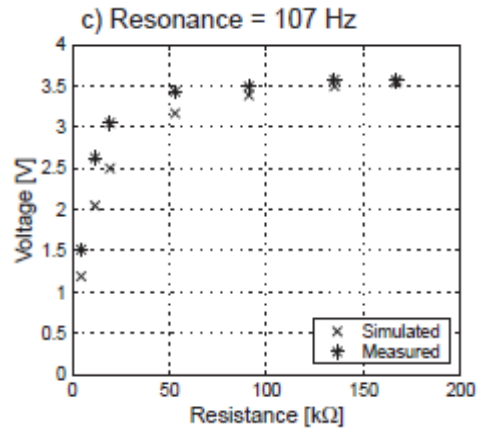
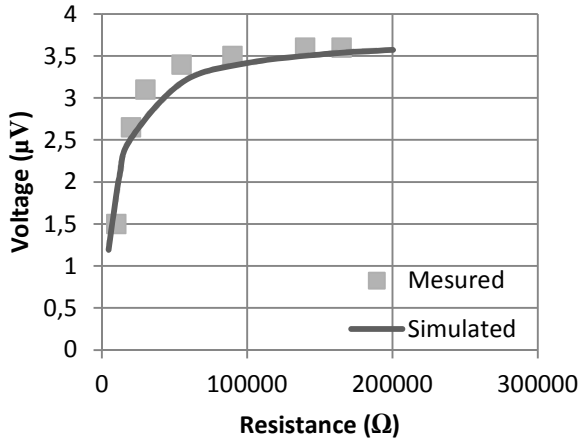
Figure B.2 Comparison of the Power output vs. resistive load for different frequencies. Thesis results on the left and original simulation on the right



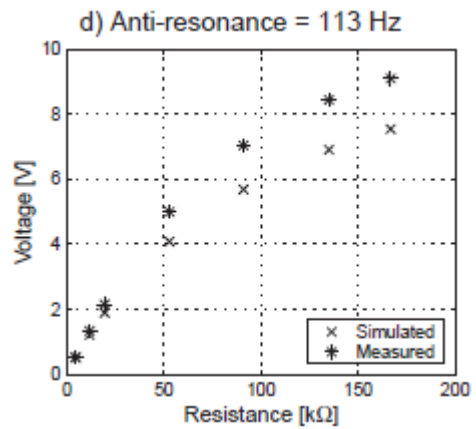
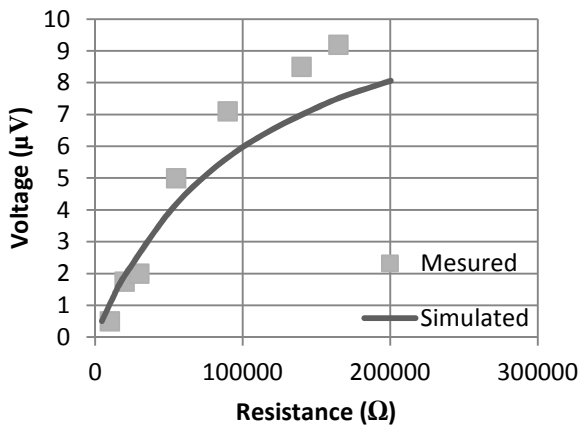
Voltage F=95Hz



Voltage F=107 Hz (Resonance)



Voltage F=113 Hz (Anti-resonance)



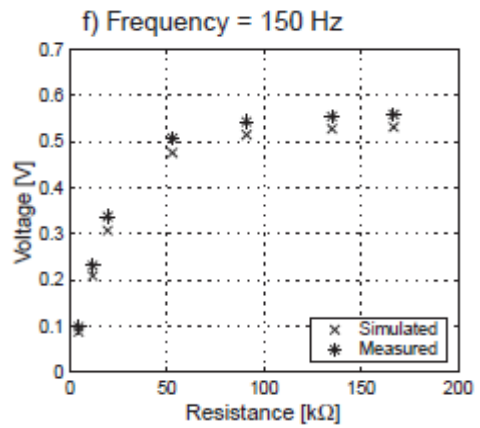
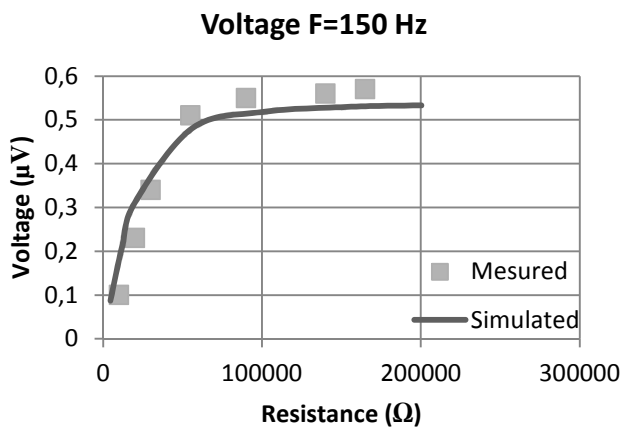
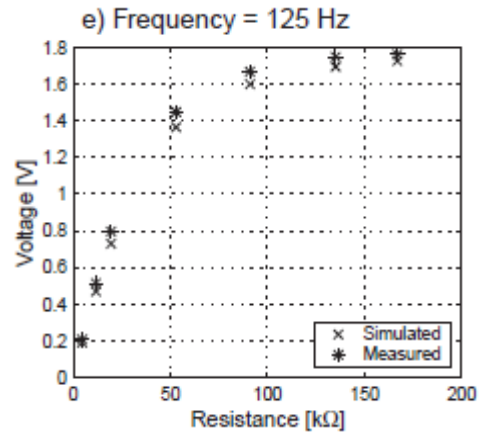
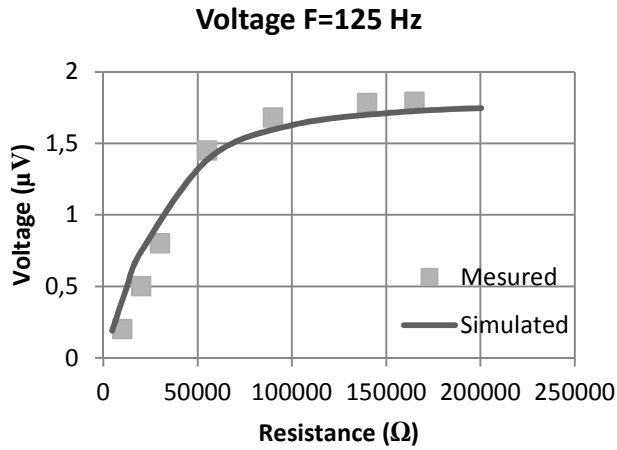
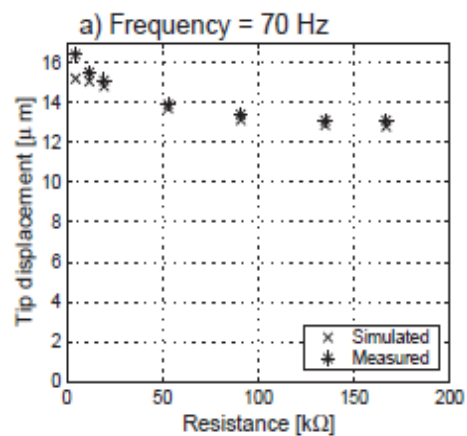
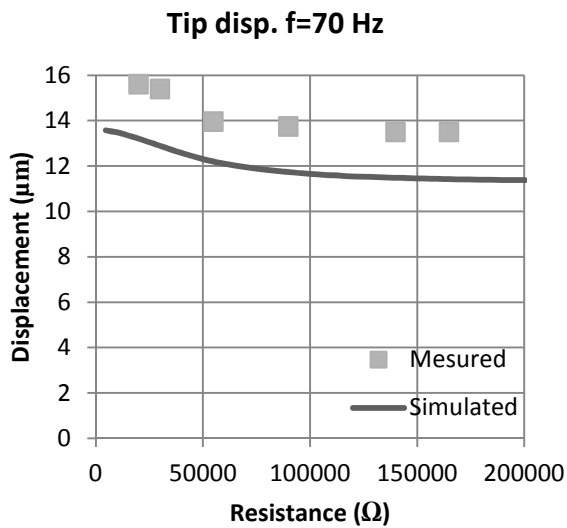
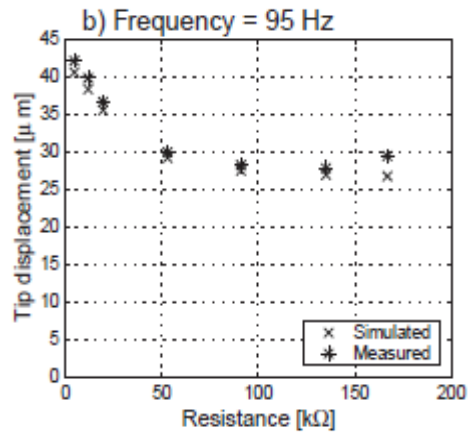
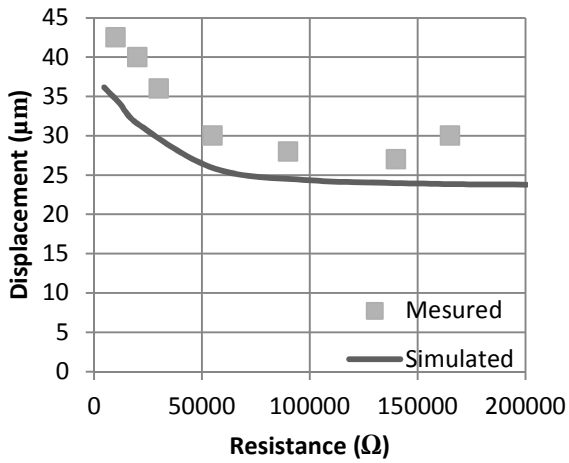


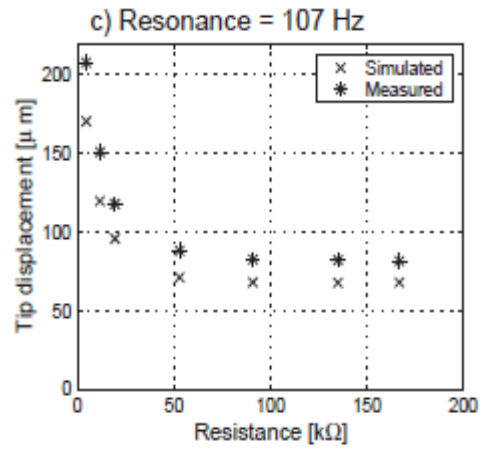
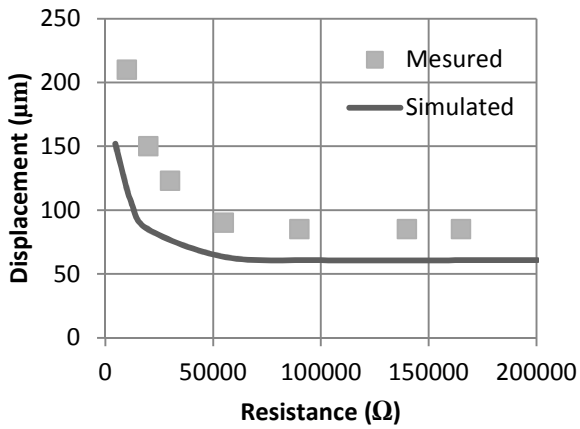
Figure B.3 Comparison of the Voltage output vs. resistive load. Thesis results on the left and original simulation on the right



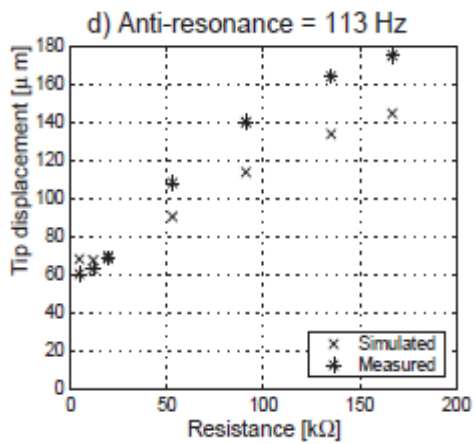
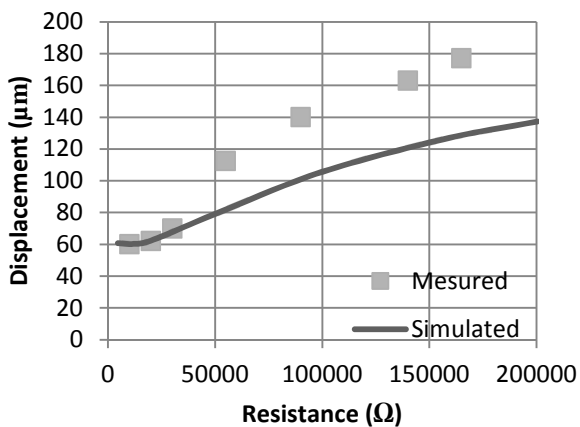
Tip disp. f=95 Hz



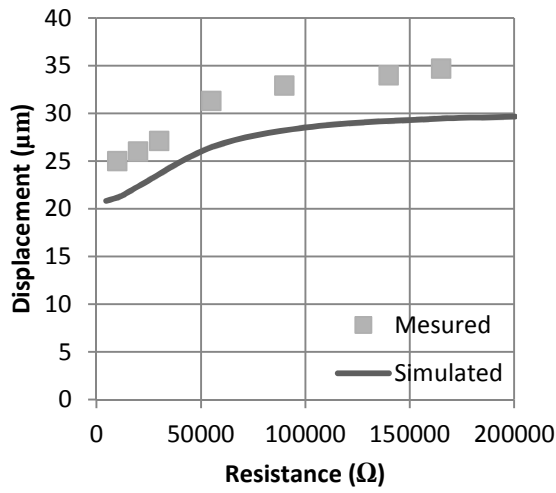
Tip disp. f=107 Hz (Resonance)



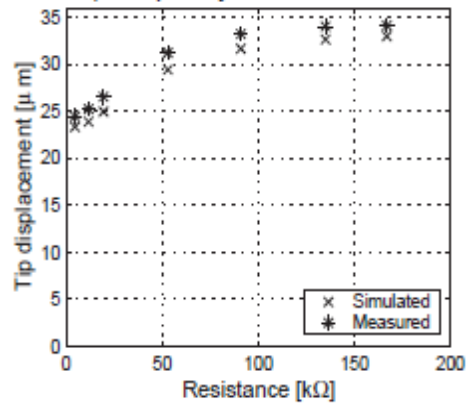
Tip disp. f=113 Hz (Anti-resonance)



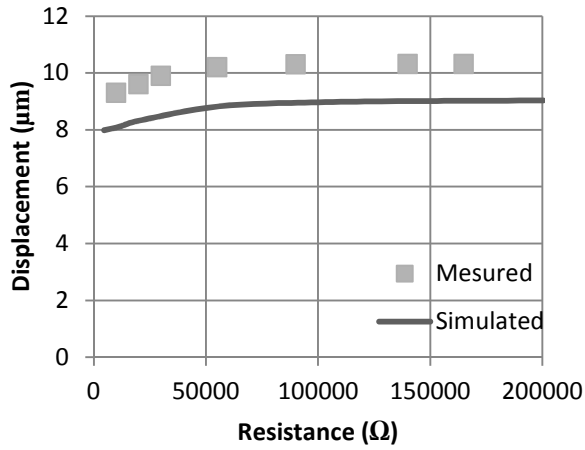
Tip disp. f=125 Hz



e) Frequency = 125 Hz



Tip disp. f=150 Hz



f) Frequency = 150 Hz

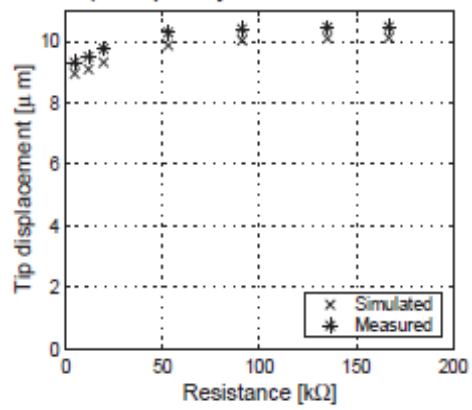


Figure B.4 Comparison of the Tip displacement vs. resistive load. Thesis results on the left and original simulation on the right